

UNIVERSITAT DE BARCELONA



UNIVERSITAT POLITÈCNICA DE CATALUNYA BARCELONATECH

Quantum Monte Carlo study of systems interacting via long-range interactions mediated by a cavity

Author:

Marta Domínguez-Navarro

Supervisors:

Grigory E. Astrakharchik[1], Abel Rojo-Francàs[2, 3]

[1] Departament de Física, Universitat Politècnica de Catalunya (UPC)
[2] Quantum Systems Unit, Okinawa Institute of Science and Technology (OIST)
[3] Departament de Física Quàntica i Astrofísica, Universitat de Barcelona (UB)

MASTER IN QUANTUM SCIENCE AND TECHNOLOGY

Universitat de Barcelona

Barcelona, July 2025

Quantum Monte Carlo study of systems interacting via long-range interactions mediated by a cavity

Marta Domínguez-Navarro

Supervised by: Grigory E. Astrakharchik[1], Abel Rojo-Francàs[2, 3]

[1] Departament de Física, Universitat Politècnica de Catalunya (UPC)
[2] Quantum Systems Unit, Okinawa Institute of Science and Technology (OIST)
[3] Departament de Física Quàntica i Astrofísica, Universitat de Barcelona (UB)

July 2025

Cavity-mediated interactions provide a versatile platform for realizing tunable long-range correlations in ultracold atomic systems. Such interactions introduce periodic, infinite-range coupling that might fundamentally alter ground-state properties. This Master's Thesis studies the many-body behavior of quantum gases with cavity-induced interactions in one dimension using Quantum Monte Carlo techniques. A pair-product trial wavefunction, constructed from the exact two-body solution, is proposed and implemented within Variational and Diffusion Monte Carlo simulations to study systems of up to 40 particles. In the absence of short-range interactions, we identify a crossover from a stable, weakly modulated phase realized for repulsive interactions to a delocalized bound state for attractive interactions, marked by clustering, loss of superfluidity, and the absence of a thermodynamic limit. The addition of short-range repulsion, either via contact interactions or fermionic statistics, restores phononic excitations and reveals a frustrated mesoscopic regime. A qualitative phase diagram is proposed to illustrate the combined effects of short- and long-range interactions, highlighting the emergence of distinct regimes with characteristic structural properties. Structure factor analysis confirms Luttinger-liquid behavior in compressible regimes and highlights the suppression of low-energy modes in attractive cases.

Keywords: Long-range interactions, Cavity-mediated interactions, Quantum Monte Carlo, One-dimensional quantum gases

Marta Domínguez-Navarro: mdominna45@alumnes.ub.edu

Acknowledgements

I would like to express my deepest gratitude to both my supervisors. Grigory Astrakharchik, for his invaluable guidance, support, and patience throughout this work. His insights, remarkable physical intuition, and expertise have been fundamental at every stage of this project. I am equally thankful to Abel Rojo-Francàs for his unwavering support, for sharing his knowledge, and for always being available to offer thoughtful comments, guidance, and discussions, even across a seven-hour time difference.

Special thanks go to Bruno Julia-Diaz for making this master's thesis possible by giving me the opportunity to work with both the ManboQu and BQMC groups. Without his support and guidance, this Master's Thesis might not have existed.

I am also sincerely grateful to my family for their constant encouragement and support, especially during the most stressful times, and to my friends for always bringing light to my life and helping to ease the burden during difficult moments.

In particular, I would like to sincerely thank Joan Hernández Tey, whose resilience through the hardest of times has inspired me to keep going no matter how difficult things become. Thank you for always listening, encouraging me, and being there through everything.

Contents

1 Introduction **1**

2 Physical Model **2**
2.1 Experimental realization . . . 2
2.2 System Hamiltonian . . . 3
2.3 One-Dimensional Geometry . . . 3

3 Numerical Methods **4**
3.1 Exact Wavefunction for two particles . . . 4
3.2 Trial Wavefunction for Many-Body Systems . . . 5
3.2.1 Bosons with long-range interaction . . . 5
3.2.2 Bosons with short- and long-range interaction . . . 5
3.2.3 Fermions with long-range interaction . . . 6
3.3 Quantum Monte Carlo Methods . . . 6
3.3.1 Variational Monte Carlo Method . . . 6
3.3.2 Diffusion Monte Carlo Method . . . 7
3.3.3 Observables . . . 8

4 Two Particle Analysis **8**
4.1 Wavefunction Structure and Symmetries . . . 9

5 Ground-state properties of an ideal Bose gas with cavity-mediated interaction **10**
5.1 Density profile and superfluid response . . . 10
5.2 Energy and thermodynamic behavior . . . 11

6 Effects of Short-Range Interactions on Cavity-Mediated Systems **13**
6.1 Density Profile and Frustrated Ordering . . . 14
6.2 Energy Scaling and Qualitative Phase Diagram . . . 16
6.3 Structure Factor and Low-Momentum Excitations . . . 17

7 Conclusions and Outlook **18**

References **23**

A Theoretical Model **i**

B Imaginary Time Evolution and Quantum Monte Carlo **ii**
B.1 Imaginary Time Evolution . . . ii
B.2 Variational Monte Carlo Method . . . iii
B.3 Diffusion Monte Carlo Method . . . iv
B.4 Statistical Error Analysis and Correlation Effects . . . vi

C Numerical Benchmarks **vii**
C.1 Harmonic Oscillator . . . vii
C.2 Lieb-Liniger Model . . . ix

D Contact Interaction via Bethe–Peierls Boundary Condition (1D) **x**

E Logarithmic derivatives for local energy and drift force calculations xi

F Comparing energy results using VMC and DMC methods xii

G Structure Factor Comparison: Contact Interaction vs. Contact and Long-Range Interaction xiii

1 Introduction

The rapid development of quantum simulators has transformed the study of complex many-body phenomena by enabling their realization in highly controllable experimental platforms. Systems such as ultracold atomic gases [Gre+02], trapped ions [PC04], and others offer unprecedented control over system parameters, facilitating the engineering of tailored quantum Hamiltonians and the exploration of exotic quantum phases [Lew+07; GB17].

While short-range interactions are highly tunable and have been extensively studied, both theoretically [Gre+02] and experimentally [Jak+98], particularly in optical lattices, long-range interactions have attracted sustained interest due to their ability to induce a plenitude of collective behavior, where phases display different types of orders simultaneously [BP12]. Theoretical studies have shown that such interactions can lead to phenomena such as supersolidity and non-equilibrium phase transitions, motivating ongoing efforts to explore their role in quantum many-body systems [Lah+09; Bar+12].

Among the various schemes proposed to realize long-range interactions in quantum gases, high-finesse optical cavities offer a potent and versatile platform, in these setups, atoms coherently scatter photons into a common cavity mode, resulting in effective infinite-range interactions mediated by the light field. These interactions are highly tunable in both strength and symmetry and have been shown to drive phenomena such as self-organization [NSD08], collective friction [VJD05; BCV03], and symmetry-breaking phase transitions [GLG10].

A key experimental demonstration of these effects was provided by Mottl et al. [Mot+12], who observed roton-like mode softening in the excitation spectrum of a Bose-Einstein condensate coupled to a standing-wave cavity. The divergence of the susceptibility at finite momentum was interpreted as a precursor to crystalline order. Such mode softening has been proposed as a possible route to supersolidity, where superfluidity coexists with density modulation. Motivated by these early results, subsequent experiments have significantly broadened the scope of cavity QED. These include the realization of multimode cavities [Lan+16], the implementation of dynamically tunable optical lattices to explore driven phase transitions [Kli+15], and the development of programmable optomechanical arrays of levitated particles [Vij+24].

Despite these experimental breakthroughs, theoretical studies must keep pace to provide a comprehensive understanding of cavity-mediated long-range interactions. Effective models describing these systems often involve nonlocal and nonlinear couplings, which challenge standard analytical and numerical approaches. In particular, mean-field and perturbative methods are generally inadequate in strongly interacting regimes. In this context, numerical techniques, especially Quantum Monte Carlo (QMC) methods, offer a powerful non-perturbative framework for investigating ground-state properties and correlation functions in correlated quantum gases. Previous works have employed Monte Carlo methods to study cavity-mediated long-range interactions in lattice systems, specifically within extended Bose-Hubbard models [Dog+16; KP22]. To the best of our knowledge, no exact solution was given to the many-body problem in continuum geometry.

The main goal of this thesis is to study the ground-state properties of a one-dimensional quantum gas with cavity-mediated long-range interactions, based on the results found in Ref. [Mot+12], where they achieve a periodic infinite-ranged interaction. To achieve this, we use Quantum Monte Carlo techniques, specifically Variational and Diffusion Monte Carlo, to numerically simulate systems with up to 40 particles. Both these methods allow us to obtain accurate estimates of observables such as the ground-state energy, density profiles, and static structure factor. Our analysis includes the study of different systems: the ideal Bose gas, a weakly interacting Bose gas, and a spinless ideal Fermi gas, each subject to the same cavity-mediated interaction. This comparative approach enables us to identify how long-range correlations manifest differently depending on the underlying quantum statistics.

This Master's Thesis is structured as follows: In Section 2, we introduce the physical context of the cavity setup and present the effective model Hamiltonian, together with the approximations used to reduce the system to a one-dimensional description. Section 3 outlines the numerical techniques used, with particular attention to the construction of the trial wavefunctions and the implementation of the Monte Carlo algorithms. Building on these foundations, we present our first results in Section 4, where we analyze the simple case of two particles to get a first look into the effects of the cavity-mediated interaction in a quantum system and to also use for the construction of the trial wavefunction in the many-body case. In Section 5, we extend the analysis to many-body systems of non-interacting bosons, characterizing the ground-state energy, density profiles, and static structure factor as a function of particle number. To further study the stability and properties of the long-range interaction in other systems, in Section 6, we incorporate additional short-range physics, contact interactions for bosons, and Pauli's exclusion constraint for fermions, and study how these contributions affect the system's behavior in the presence of the long-range cavity potential. Finally, Section 7 summarizes the main results obtained and future ventures.

2 Physical Model

In this first section, we present the physical model that forms the basis of our numerical study. We begin by reviewing the key features of the experimental setup of Ref. [Mot+12], where ultracold atoms are coupled to a single-mode optical cavity to realize tunable long-range interactions. We then introduce the full microscopic Hamiltonian describing the light-matter system, followed by a dimensional reduction leading to a simplified one-dimensional model in dimensionless units. This serves as the starting point for all the following numerical simulations.

2.1 Experimental realization

The experiment of Ref. [Mot+12] demonstrated that a system of ultracold ^{87}Rb atoms confined within an optical cavity can realize effective long-range interactions mediated by a quantized light field. These interactions were strong and tunable enough to generate signs of a quantum phase transition from a Bose-Einstein condensate to a supersolid phase, characterized by the coexistence of superfluidity and crystalline density order.

The experimental setup is based on a high-finesse Fabry–Pérot interferometer, consisting of two parallel, highly reflective mirrors that define an optical cavity. This cavity supports a discrete set of electromagnetic modes: standing waves that satisfy boundary conditions determined by the mirror spacing. Due to it being high finesse, only the mode nearest in frequency to the resonant one, characteristic of the cavity, becomes significantly populated. This mode is what mediates the interaction between atoms.

A transverse laser beam, referred to as *pump*, far red-detuned from the atomic transition, illuminates the atomic cloud. While the atoms remain in their electronic ground-state, the far-detuned field induces oscillating electric dipole moments in the atoms at the pump frequency. These dipoles scatter photons into the resonant cavity mode, populating the characteristic cavity mode. The resulting intracavity field generates a spatially modulated potential via the ac Stark effect, which in turn affects all atoms within the cavity [MR05]. Since all atoms couple to the same mode, the interaction is inherently global: the cavity field is able to link the motion of distant atoms with each other.

Remarkably, the experiment achieves a tunable long-range interaction, whose strength can be controlled via the intensity of the pump laser and the detuning between the pump and the cavity resonance. This experimental setup enabled the observation of roton-like mode

softening, which was interpreted as a precursor to a transition toward a crystalline state that still supported superfluidity, both hallmarks of a supersolid phase, as previously predicted and analyzed in Refs. [NSD08; Nag+10].

2.2 System Hamiltonian

We consider a system inspired by the experimental setup of Ref. [Mot+12], where a Bose-Einstein condensate (BEC) is coupled to a single-mode optical cavity. The theoretical framework follows Refs. [MR05; MMR08], which generalize the Jaynes-Cummings model to many-body systems of ultracold atoms by treating both the cavity field and the atomic motion quantum mechanically.
After applying a series of approximations and adiabatic eliminations (see Appx. A), the system can be described by an effective Hamiltonian of the form

$$\hat{H}_{\text{eff}} = \hat{H}_A + \hat{V}_{\text{int}}, \tag{2.1}$$

where $\hat{H}_A$ accounts for the atomic kinetic energy, external trapping, and contact interactions, and $\hat{V}_{\text{int}}$ describes the cavity-mediated long-range interactions.
The interaction potential takes the form

$$\hat{V}_{\text{int}} = V_0 \int d^3\mathbf{r}\, d^3\mathbf{r}'\, \hat{\Psi}^\dagger(\mathbf{r})\hat{\Psi}^\dagger(\mathbf{r}') \cos(k_L x)\cos(k_L z)\cos(k_L x')\cos(k_L z')\hat{\Psi}(\mathbf{r})\hat{\Psi}(\mathbf{r}'), \tag{2.2}$$

where $\hat{\Psi}(\mathbf{r})$ is the bosonic field operator, and $k_L = 2\pi/\lambda$ is the wavevector associated with the pump laser. The interaction strength V_0 is given by $V_0 \approx \hbar\frac{\eta^2}{\Delta_c - U_0\mathcal{B}_0}$. Here, η is the two-photon Rabi frequency, Δ_c is the detuning between the pump laser and cavity resonance, U_0 is the single-atom light shift, and $\mathcal{B}_0$ is the mean-field expectation value of the bunching parameter in steady state.
The atomic Hamiltonian is given by

$$\hat{H}_A = \int d^3\mathbf{r}\, \hat{\Psi}^\dagger(\mathbf{r}) \left[-\frac{\hbar^2\nabla^2}{2m} + V_p \cos^2(k_L z) + \frac{g}{2}\hat{\Psi}^\dagger(\mathbf{r})\hat{\Psi}(\mathbf{r}) \right] \hat{\Psi}(\mathbf{r}), \tag{2.3}$$

where V_p is the depth of the static optical lattice along z, and $g = 4\pi\hbar^2 a/m$ characterizes the contact interactions with a the s-wave scattering length.
The total effective Hamiltonian thus retains the kinetic and contact interaction terms of a conventional BEC, but now incorporates a nonlocal interaction that is both periodic and long-ranged. Crucially, this interaction depends explicitly on the absolute positions of the atoms rather than their relative separations, breaking Galilean invariance. Due to the spatial structure inherited from the cavity and pump modes, atoms separated by integer multiples of the cavity wavelength interact identically, highlighting the infinite-range and periodic nature of the induced interactions.

2.3 One-Dimensional Geometry

The full three-dimensional Hamiltonian derived above serves as the starting point for our analysis. To make the simulations of the system properties more accessible, we consider a simplified version of the many-body problem, in which the atomic motion is restricted to one dimension (x-axis). This approximation corresponds to the situation of a deep transverse optical lattice, which is equivalent to having a large V_p in Eq. (2.3) so that the separation between the transverse levels becomes large and they cannot be excited.

The resulting effective one-dimensional Hamiltonian reads

$$H_{1\mathrm{D}} = \sum_{i=1}^{N} \left(-\frac{\hbar^2}{2m} \frac{\partial^2}{\partial x_i^2} \right) + \sum_{i<j} g\, \delta(x_i - x_j) + \sum_{i<j} V_0 \cos\left(k_{\mathrm{L}} x_i\right) \cos\left(k_{\mathrm{L}} x_j\right), \tag{2.4}$$

where N is the number of atoms, $g = -2\hbar^2/(m a_{1\mathrm{D}})$ is the effective one-dimensional coupling constant, and $a_{1\mathrm{D}}$ is the one-dimensional s-wave scattering length. The last term describes a cavity-mediated long-range interaction with amplitude V_0 and the wavevector k_{L}. To model repulsive contact interactions, we choose $a_{1\mathrm{D}} < 0$, such that $g > 0$.
The underlying optical lattice sets natural units for the energy and length to compare with. We choose the cavity wavelength λ as the unit of length and define the natural energy scale as

$$\varepsilon = \frac{\hbar^2}{m\lambda^2},$$

which, up to a numerical factor, corresponds to the *recoil* energy $E_{\mathrm{r}} = \hbar^2 k_L^2/(2m)$.
The cavity-mediated interaction term in Eq. (2.4) in one-dimensional geometry is written as

$$V_{\mathrm{int}}(x_i, x_j) = V_0 \cos\left(\frac{2\pi}{\lambda} x_i\right) \cos\left(\frac{2\pi}{\lambda} x_j\right), \tag{2.5}$$

and possesses an infinite-range character of the interaction. Interaction potential (2.5) breaks translational invariance and introduces a periodic structure into the system, playing a central role in its self-organization dynamics.

3 Numerical Methods

In this section, we outline the numerical methods used throughout this work, with a focus on how they are applied to study the quantum system with the cavity-mediated long-range interaction presented in the previous section with Hamiltonian Eq. (2.4). Our approach consisted of three numerical methods: Imaginary Time Evolution (ITE) to extract the two-body wavefunction; Variational Monte Carlo (VMC) method to explore the many-body system using a variational ansatz based on the two-body solution; and Diffusion Monte Carlo (DMC) method to calculate exact estimates, within statistical error, of the energy in several cases and to validate our variational results.
A more technical and detailed description of the numerical algorithms is provided in Appxs. B and C, which also include benchmarking results for selected test cases. The full implementation of all numerical methods discussed in this section is available in a public GitHub repository [Dom].

3.1 Exact Wavefunction for two particles

To obtain the ground-state energy E_0 and wavefunction $\psi_2(x_1, x_2)$, we solve the Schrödinger equation in imaginary time for two particles interacting via the cavity-mediated potential given by Eq. (2.5) in a one-dimensional box with periodic boundary conditions. We evolve the system in imaginary time by replacing $t \to -i\tau/\hbar$ in the time-dependent Schrödinger equation. We start from a continuous and square-integrable trial wavefunction $\psi(x_1, x_2, \tau = 0)$ and numerically solve the differential equation (for more details see Appx. B). As the imaginary time increases, higher-energy components decay faster than the ground-state component, and the system is projected to the ground-state of the Hamiltonian (up to normalization):

$$\psi(x_1, x_2, \tau) \xrightarrow{\tau \to \infty} \psi_2(x_1, x_2) e^{-E_0 \tau} \tag{3.1}$$

The resulting wavefunction is sampled on a discrete spatial grid and interpolated using a spline. This result plays two main roles in our analysis: it provides physical insight into the two-body correlations induced by the cavity interaction, and it serves as a building block for constructing the many-body trial wavefunction we used in Variational and Diffusion Monte Carlo simulations.

3.2 Trial Wavefunction for Many-Body Systems

To construct a trial wavefunction suitable for studying the many-body system, it is common to use the Jastrow ansatz, which encodes pairwise correlations in homogeneous quantum systems,

$$\Psi_{\text{Jastrow}}(\mathbf{x}) = \prod_{i<j} f(|x_i - x_j|), \tag{3.2}$$

where the pairwise function $f(|x_i - x_j|)$ depends only on the interparticle distance $|x_i - x_j|$, assuming translational invariance of the interaction potential.
In our case, however, the cavity-mediated interaction explicitly breaks translational invariance, and thus a standard Jastrow form would fail to fully capture the physics of the interaction. Instead, we adopt a position-resolved ansatz based on the two-body wavefunction $\psi_2(x_i, x_j)$ that depends on the positions of both particles. This allows us to accurately capture the position-dependent correlations induced by the periodic long-range interaction.

3.2.1 Bosons with long-range interaction

Using the solution to the two-body case, we use the numerically computed wavefunction $\psi_2(x_i, x_j)$ to build a trial wavefunction for many-body simulations. Following the spirit of Jastrow-type wavefunctions, we extend the pairwise structure by taking the product over all pairs of particles:

$$\Psi^{(\text{B})}_{\text{LR}}(x_1, \ldots, x_N) = \prod_{i<j} \psi_2(x_i, x_j). \tag{3.3}$$

This form allows us to retain the spatial correlations induced by the cavity-mediated interaction. Since the two-particle wavefunction depends on the positions of both particles rather than just their relative distance, Eq. (3.3) can capture the non-translationally-invariant structure for the many-body case.
However, Eq. (3.3) only includes the cavity interaction. To explore more physical regimes, we add two terms: one to account for contact interactions, and another to describe fermionic statistics. These extra factors are multiplied into the wavefunction and can be added or not depending on the parameters we choose.

3.2.2 Bosons with short- and long-range interaction

To incorporate short-range repulsion, which is represented in Eq. (2.4) by a delta function we propose the following expression for the trial wavefunction

$$\Psi^{(\text{B})}_{\text{SR+LR}}(x_1, \ldots, x_N) = \prod_{i<j} \psi_2(x_i, x_j) \prod_{i<j} f_{2B}(|x_i - x_j|), \tag{3.4}$$

where $f_{2B}(x) = \cos\left[k_c \left(|x| - \frac{L}{2}\right)\right]$, which is chosen to satisfy the Bethe-Peierls boundary condition $\left.\frac{f'_{2B}(x)}{f_{2B}(x)}\right|_{x\to 0} = -\frac{1}{a_{1D}}$ which allows us to include the effect of contact interactions

without having to deal with the singular nature of the delta potential directly (for more details see Appx. D). As well $f_{2B}(x)$ satisfies the periodic boundary conditions, as $f'_{2B}\left(\frac{L}{2}\right) = 0$.

3.2.3 Fermions with long-range interaction

In addition to short-range repulsion, we also explore the effect of quantum statistics. More specifically, we want to compare our bosonic system to its fermionic counterpart.
According to Bose-Einstein statistics, the many-body wavefunction must be symmetric under the exchange of any two particles. Indeed, wavefunctions Eqs. (3.3) and (3.4) preserve bosonic symmetry

$$\begin{aligned}\Psi^{(\mathrm{B})}_{\mathrm{LR}}(x_1,...,x_i,...,x_j,...,x_N) &= \Psi^{(\mathrm{B})}_{\mathrm{SLR}}(x_1,...,x_j,...,x_i,...,x_N)\\ \Psi^{(\mathrm{B})}_{\mathrm{SR+LR}}(x_1,...,x_i,...,x_j,...,x_N) &= \Psi^{(\mathrm{B})}_{\mathrm{SR+LR}}(x_1,...,x_j,...,x_i,...,x_N),\end{aligned} \tag{3.5}$$

under the exchange of any two particles i and j, where N is the total number of particles in the system..
However, for Fermi-Dirac statistics, the many-body wavefunction must be antisymmetric under two-particle exchange, which implies that

$$\Psi^{(\mathrm{F})}_{\mathrm{LR}}(x_1,...,x_i,...,x_j,...,x_N) = -\Psi^{(\mathrm{F})}_{\mathrm{LR}}(x_1,...,x_j,...,x_i,...,x_N) \tag{3.6}$$

To introduce the antisymmetrization of the wavefunction we consider the ground-state wavefunction of an ideal Fermi gas in the absence of interaction as a Slater determinant, which in one dimension takes the form of a Vandermonde determinant and can be written as a pair product

$$\Psi^{(\mathrm{F})}(x_1,\dots,x_N) = \frac{1}{\sqrt{N!}}\det\left[e^{ik_j x_i}\right]_{i,j=1}^{N} = \text{const}\times\prod_{i<j}\sin\left[\frac{\pi}{L}(x_i-x_j)\right], \tag{3.7}$$

where $k_j = \frac{2\pi}{L}n_j$, and the n_j are integers labeling the N lowest-energy single-particle states. In order to take the long-range interactions into account, we use the following wavefunction to describe fermions,

$$\Psi^{(\mathrm{F})}_{\mathrm{LR}}(x_1,\dots,x_N) = \prod_{i<j}\psi_2(x_i,x_j)\prod_{i<j}\sin\left[\frac{\pi}{L}(x_i-x_j)\right]. \tag{3.8}$$

This wavefunction vanishes whenever any two particles are at the same position, enforcing the nodal structure required for a system of spinless fermions.

Bosons LR	$\Psi^{(\mathrm{B})}_{\mathrm{LR}}(x_1,\dots,x_N) = \prod_{i<j}\psi_2(x_i,x_j)$
Bosons SR+LR	$\Psi^{(\mathrm{B})}_{\mathrm{SR+LR}}(x_1,\dots,x_N) = \prod_{i<j}\psi_2(x_i,x_j)\prod_{i<j}\cos\left[k_c\left(\lvert x_i-x_j\rvert-\frac{L}{2}\right)\right]$
Fermions LR	$\Psi^{(\mathrm{F})}_{\mathrm{LR}}(x_1,\dots,x_N) = \prod_{i<j}\psi_2(x_i,x_j)\prod_{i<j}\sin\left[\frac{\pi}{L}(x_i-x_j)\right]$
Fermions SR+LR	No contact interaction can be added because spinless fermions do not interact via s-wave scattering

Table 1: Table summarizing the trial wavefunctions employed for different interaction regimes and quantum statistics. "LR" denotes long-range interactions given by Eq. (2.5), while "SR" refers to contact interactions modeled by a delta-function potential.

3.3 Quantum Monte Carlo Methods

3.3.1 Variational Monte Carlo Method

Once the trial wavefunction is defined, the Variational Monte Carlo (VMC) method can be used to study the many-body ground-state properties of the system. The VMC technique

is the main numerical method used in this work, as it allows us to evaluate both energetic and structural observables efficiently for a broad range of particle numbers and interaction strengths.
The method is based on the variational principle, which states that the expectation value of the Hamiltonian over any wavefunction Ψ_T different from the ground-state gives an upper bound to the true ground-state energy:

$$E_0 \leq \frac{\langle \Psi_T | \hat{H} | \Psi_T \rangle}{\langle \Psi_T | \Psi_T \rangle}. \tag{3.9}$$

In practice, we sample configurations $\mathbf{R} = (x_1, \ldots, x_N)$ according to the distribution $|\Psi_T(\mathbf{R})|^2$ using the Metropolis algorithm. For each configuration, we compute the local energy:

$$E^{\text{loc}}(\mathbf{R}) = \frac{1}{\Psi_T(\mathbf{R})} \hat{H} \Psi_T(\mathbf{R}) = E^{\text{loc}}_{\text{kin}}(\mathbf{R}) + E^{\text{loc}}_{\text{int}}(\mathbf{R}). \tag{3.10}$$

To compute the kinetic energy, we use logarithmic derivatives. Below, we show the expression for the two-body part of the wavefunction, $\psi_2(x_k, x_i)$, which is interpolated using splines; the other contributions (from contact interaction and Fermi statistics) are treated analytically and can be differentiated exactly:

$$E^{\text{loc}}_{\text{kin}}(\mathbf{R}) = -\frac{\hbar^2}{2m} \sum_{k=1}^{N} \left[\left(\sum_{i \neq k} \frac{\partial_k \psi_2(x_k, x_i)}{\psi_2(x_k, x_i)} \right)^2 + \sum_{i \neq k} \left(\frac{\partial_k^2 \psi_2(x_k, x_i)}{\psi_2(x_k, x_i)} - \left(\frac{\partial_k \psi_2(x_k, x_i)}{\psi_2(x_k, x_i)} \right)^2 \right) \right], \tag{3.11}$$

where $\psi_2(x_k, x_i)$ denotes the pairwise component of the wavefunction and $\partial_k \psi_2(x_k, x_i)$ is the partial derivative of the spline over the x_k coordinate. The complete expression and implementation details for the kinetic energy calculation are presented in Appx. E.
On the other hand, the interaction energy is calculated directly from the pairwise potential, as it is diagonal in the coordinate representation:

$$E^{\text{loc}}_{\text{int}}(\mathbf{R}) = \sum_{i<j} V(x_i, x_j), \quad \text{where} \quad V(x_i, x_j) = V_0 \cos\left(\frac{2\pi}{\lambda} x_i\right) \cos\left(\frac{2\pi}{\lambda} x_j\right). \tag{3.12}$$

3.3.2 Diffusion Monte Carlo Method

As close as the Variational Monte Carlo (VMC) method may bring us to the true ground-state, its estimates for the energy are always an upper bound, unless the trial wavefunction exactly coincides with the true ground-state wavefunction. However, in the absence of an analytical solution for our system, it is difficult to assess the accuracy of the VMC approximation.
To address this, we study selected cases using the Diffusion Monte Carlo (DMC) method, which yields the exact ground-state energy of a system within statistical uncertainty. The DMC method thus, provides a valuable benchmark for validating the VMC results.
The DMC approach is based on imaginary time evolution, and projecting out the ground-state state, the same basis used to first solve the two-body system. However, rather than solving the high-dimensional Schrödinger equation directly, the DMC method formulation uses the path integral formalism of quantum mechanics [FHS10] and evaluates the resulting integrals stochastically via Monte Carlo sampling.
In our DMC simulations, we employ importance sampling to enhance convergence. Specifically, we use the same trial wavefunctions proposed for the VMC calculations (Table 1) as guiding functions. While DMC provides more accurate energy estimates, it is also significantly more computationally expensive. Therefore, we restrict our DMC study to a subset

of cases, focusing on validating the overall behavior observed in the VMC results. Despite minor quantitative differences, we find that the qualitative features of the system are well captured by the trial wavefunction in most cases. A visual comparison between VMC and DMC outcomes is presented in Appx. F.

3.3.3 Observables

In addition to the energy, we compute a number of observables to describe spatial correlations in the system.
First, we introduce the density profile $n(x)$ to quantify how particles are distributed along the box

$$n(x) = \frac{1}{N} \left\langle \sum_{i=1}^{N} \delta(x - x_i) \right\rangle \tag{3.13}$$

where $\langle ... \rangle$ denotes the ground-state averaging.
We also calculate the pair distribution function $g^{(2)}(x, x')$, which measures the probability of finding a pair of particles one occupying x and the other x', or vice versa.

$$g^{(2)}(x, x') = \frac{2}{N(N-1)} \left\langle \sum_{i<j} \delta(x - x_i)\delta(x' - x_j) \right\rangle, \tag{3.14}$$

due to the absence of Galilean invariance, $g^{(2)}(x, x')$ depends on two positions (x, x') and cannot be reduced to a function depending on the relative positions $(x - x')$. This function captures short and long-range spatial correlations.
We also calculate the static structure factor $S(k)$, which is a response function that gives information about how a system's density in equilibrium is affected by a weak perturbation of wavelength $2\pi/k$.

$$S(k) = \frac{1}{N} \left\langle \sum_{i,j} e^{ik(x_i - x_j)} \right\rangle. \tag{3.15}$$

It quantifies the correlations in momentum space and can be used to provide information on the excitation spectrum.
Finally, we calculate the Leggett bound [Leg98] as a way to quantify superfluid response. The Leggett bound gives us an upper limit to the superfluid fraction:

$$\frac{\rho_S}{\rho} \leq \frac{1}{\langle n(x) \rangle \, \langle \frac{1}{n(x)} \rangle}, \tag{3.16}$$

where $n(x)$ is the density profile defined in Eq. (3.13).
These observables together allow us to interpret the energy results and identify signatures of localization, clustering, or ordering driven by the interaction parameters.
All Monte Carlo results carry statistical uncertainties inherent to the sampling process. These are estimated following the procedure outlined in Appx. B.4, but are typically smaller than the symbol size and thus not visible in the plots we show in this Master's Thesis.

4 Two Particle Analysis

Now that we have defined the full Hamiltonian and the numerical methods used throughout this thesis, we begin the actual analysis of the system. We choose as a starting point the

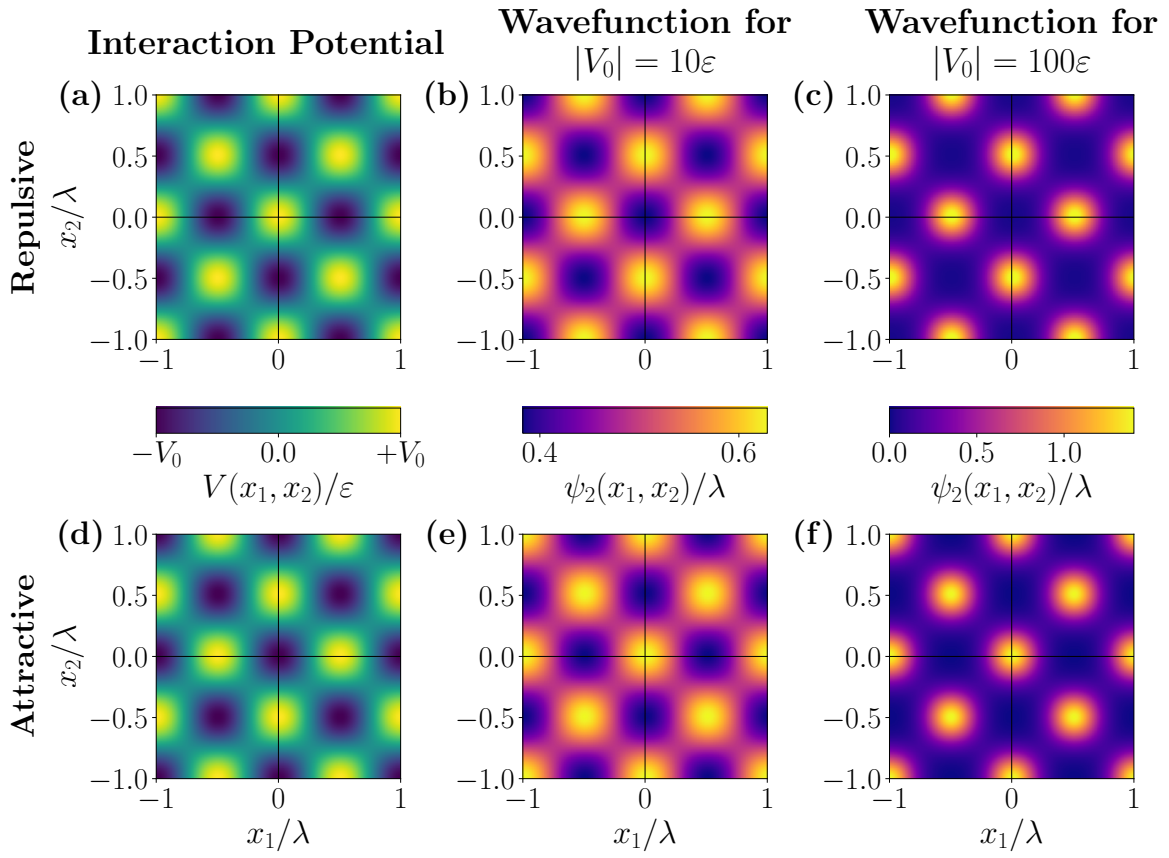

Figure 1: Long-range interaction potential and two-body wavefunctions. Panel (a) and (d): Cavity-mediated long-range interaction given by Eq. (2.5) for the repulsive and attractive cases, respectively. Panels (b) and (c): Ground-state two-body wavefunction $\psi(x_1, x_2)$ for repulsive interactions, obtained via imaginary time evolution, at interaction strengths $V_0 = 10\varepsilon$ and $V_0 = 100\varepsilon$. Panels (e) and (f): Ground-state two-body wavefunctions for the corresponding attractive case.

simplest case: two particles in a box with periodic boundary conditions, interacting only via long-range interactions. Due to the simplicity of the system, we can find the exact wavefunction and energy using the Imaginary Time Evolution (ITE) scheme.

Although seemingly trivial, the two-particle case is interesting for several reasons. On one hand, it represents the minimal setting in which interaction appears, and thus, interesting physical behaviors emerge. On the other hand, since this system is computationally tractable, it also serves as a starting point to begin working in a many-body context as explained in the previous section with the trial wavefunction.

4.1 Wavefunction Structure and Symmetries

As a preliminary study of how the interaction affects the wavefunction structure, we show in Fig. 1 (a)–(f) the interaction potential, and the resulting two-body wavefunction for $|V_0| = 10\varepsilon$ and $|V_0| = 100\varepsilon$ in both the attractive, $V_0 > 0$, and repulsive, $V_0 < 0$, cases.

One observes how a characteristic "checkerboard" pattern emerges. Remarkably, this pattern in the wavefunction is opposite to the pattern in the interactions, that is, maxima in the interaction, correspond to minima in the wavefunction, and vice versa. This result reflects the system's tendency to minimize its energy by occupying the regions where the interaction between particles is minimal.

In addition, an important feature that already emerges in the two-particle case is the quali-

tative difference between repulsive and attractive interactions. By comparing Fig. 1 (b) with (e) and Fig. 1 (c) with (f), one observes that the wavefunctions exhibit identical patterns, but shifted by half a period, following the property of the potential:

$$V(x_1, x_2) = -V\left(x_1 + \frac{\lambda}{2}, x_2\right) = -V\left(x_1, x_2 + \frac{\lambda}{2}\right). \tag{4.1}$$

In the attractive case, the diagonal ($x_1 = x_2$) is strongly populated, indicating that the two particles tend to occupy the same position, similarly shifted diagonals ($x_1 = x_2 + \ell \cdot \lambda$, with $\ell = \pm 1, \pm 2, ...$) are equally populated, that is where the product of cosines is positive Eq. (2.5). In contrast, in the repulsive case, the wavefunction is suppressed along the diagonal as the particles avoid each other and preferably occupy positions separated by half a period, where the product of cosines in Eq. (2.5) is negative. The way the system lowers its energy depends on the sign of the interaction, which in turn causes a shift in the characteristic pattern of the wavefunction.

In addition to the sign of the long-range interaction, its potential amplitude V_0 also plays an important role in shaping the wavefunction. Comparing panels (b) and (c), we see that increasing $|V_0|$ from 10ε to 100ε leads to a much stronger localization of the particles within the interaction wells. For large V_0, the wavefunction fragments and resembles the ground-state of a harmonic oscillator repeated periodically across a grid of wells, following the structure of the cavity-mediated potential.

5 Ground-state properties of an ideal Bose gas with cavity-mediated interaction

Using the results obtained with VMC method, we analyze the ground-state properties of an ideal Bose gas subject exclusively to cavity-mediated long-range interactions, as described by the Hamiltonian Eq. (2.4) in the absence of short-range interactions, with $g = 0$. This simplified setting allows us to isolate the effects of the periodic, infinite-range interaction and examine its impact on observables such as the density profile, superfluid response, and energy scaling.

5.1 Density profile and superfluid response

The density profiles obtained from our Monte Carlo simulations are shown in panels Fig. 2 (a)–(b) and display clear periodic modulation for both attractive ($V_0 < 0$) and repulsive ($V_0 > 0$) interactions. These modulations reflect the underlying periodicity of the cavity-mediated interaction and break the continuous translational invariance that exists in the non-interacting Bose gas ($V_0 = 0$). Throughout this analysis, we consider systems of fixed length $L = 2\lambda$.

As the number of particles increases, the density peaks become more pronounced in both regimes, although the effect is stronger for attractive interactions. In the repulsive case, the valleys between peaks stay finite, suggesting that particles remain delocalized across the system. In contrast, the attractive case shows valleys that rapidly approach zero, indicating a strong tendency for particles to bunch together into localized regions.

Remarkably, the density profiles in the attractive regime show features reminiscent of crystalline order: sharp peaks with strongly suppressed density in between. But particles are not classically localized, that is, not all of them are clustered at the same position. Instead, the ground-state is a symmetric superposition across equivalent minima. The result is a clustered but delocalized phase that does not reach full crystallization. Throughout this Thesis, we refer to this phase as *delocalized bound state*.In the repulsive regime, the system also de-

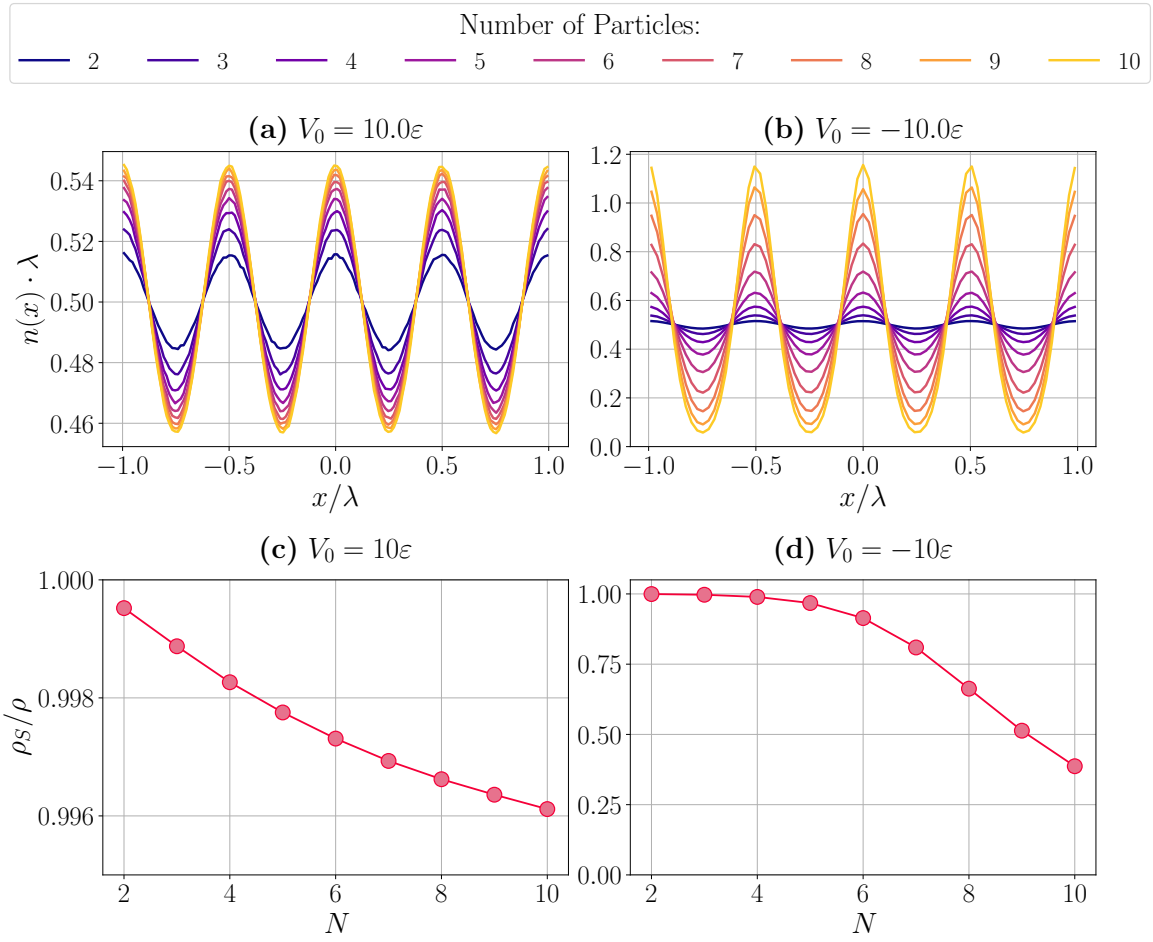

Figure 2: Density profiles $n(x)$ for particle numbers $N = 2, \ldots, 10$ obtained by Metropolis sampling, and the corresponding Leggett bounds computed using Eq. (3.16). The top row shows the density profiles $n(x)$, while the bottom row displays the associated Leggett bound. Panel (a) and (c): Repulsive interaction case with $V_0 = 10\varepsilon$. Panel (b) and (d): Attractive interaction case with $V_0 = -10\varepsilon$. All simulations are performed by fixing the length of the system $L = 2\lambda$ and changing the density $\rho = N/L$.

velops periodic density, but the particles remain connected across the system, suggesting a modulated but coherent phase.

Given the presence of periodic modulation, one might expect suppressed coherence in the system. However, the persistence of coherence, particularly in the repulsive regime, suggests the possible presence of superfluidity. To quantify it, we compute the superfluid fraction with Eq. (3.16) and using the density profiles shown in Fig. 2 (a)–(b).

The superfluid response is very different in the attractive and repulsive cases (note the different vertical scales in Fig. 2 (c)–(d)). Indeed, in the attractive regime, the superfluid fraction rapidly decays with increasing N, consistent with the idea that particles localize around the potential minima and lose phase coherence. On the other hand, the repulsive regime retains a finite Leggett bound even for large N, consistent with a delocalized phase that could still support superfluidity.

5.2 Energy and thermodynamic behavior

In order to characterize the system's behavior in different regimes, we study how the energy scales with both particle number N and interaction strength V_0, keeping the density fixed at

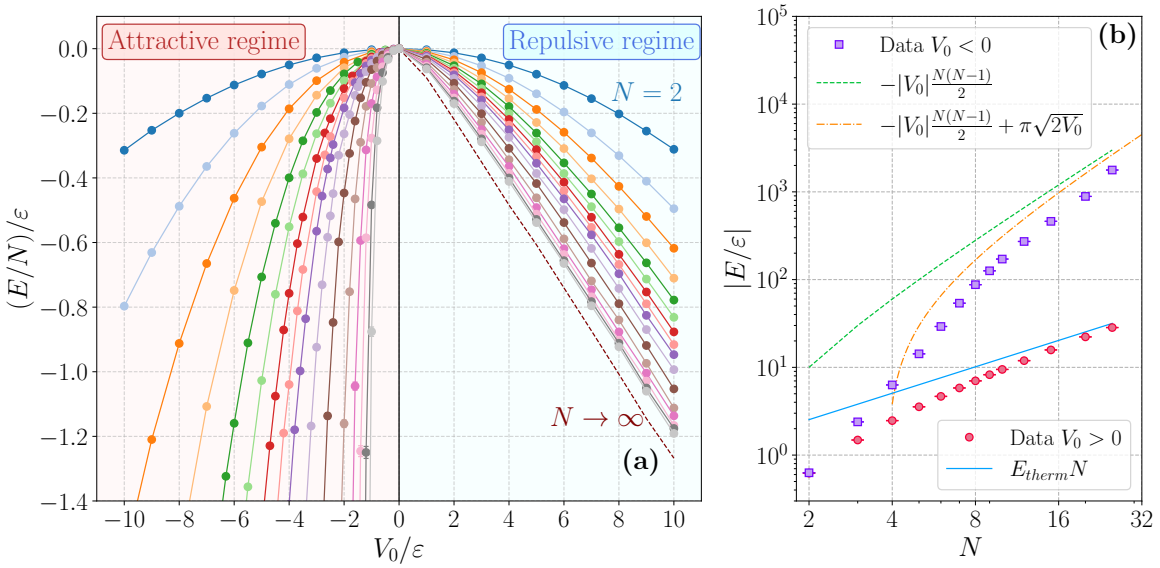

Figure 3: Ground-state energy of bosons interacting via cavity-mediated long-range potential. Symbols show VMC results. Panel (a): Energy per particle E/N as a function of interaction strength V_0 for various particle numbers $N = \{2, 3, 4, 5, 6, 7, 8, 9, 10, 12, 15, 20, 25, 30, 35, 40\}$. In the repulsive case ($V_0 > 0$), an extrapolated estimate of the thermodynamic limit is shown as a dashed maroon line. In contrast, the attractive case ($V_0 < 0$) leads to a divergent energy. Panel (b): Absolute value of the energy, $|E|$, for the specific case of $|V_0| = 10\varepsilon$ as a function of the number of particles, N, for both interaction signs, compared to the asymptotic scalings law: Eq. (5.4) for the attractive case, and $E_{th}N$ for the repulsive one. All simulations are performed at constant density $\rho = 1\lambda^{-1}$ and changing the length $L = N/\rho$.

$\rho = 1\lambda^{-1}$. Fig. 3 (a) shows the energy per particle E/N as a function of V_0, while Fig. 3 (b) displays the total energy $E(N)$ as a function of the number of particles for fixed $|V_0| = 10\varepsilon$. In the absence of long-range interaction, $V_0 = 0$, we recover the trivial result for a homogeneous ideal Bose gas:

$$E = 0. \tag{5.1}$$

As the long-range interaction is introduced, the energy, E, becomes negative both in the attractive and repulsive regimes, reflecting the formation of correlated states in the regions where the interaction potential is negative. While this lowering of energy is often associated with spatial clustering, in this case, the particles remain delocalized and distribute themselves across the periodic minima of the cavity-mediated potential.

In the repulsive regime, $V_0 > 0$, we observe that as the number of particles, N, increases, the energy per particle converges toward a constant value:

$$\lim_{N\to\infty} \frac{E(N)}{N} = \text{const}, \tag{5.2}$$

indicating that the system's energy is extensive and possesses a well-defined thermodynamic limit. To extract this limit, we perform a linear extrapolation of E/N versus $1/N$ for each value of V_0, with the intercept at $1/N = 0$ corresponding to the infinite-particle limit. The extrapolation to the thermodynamic limit is shown in Fig. 3 (a) as the dashed maroon line.

In Fig. 3 (b) we show the dependence of the absolute value of the ground-state energy on the number of particles in two characteristic cases, $V_0 = 10\varepsilon$ (repulsion) and $V_0 = -10\varepsilon$ (attraction). In the repulsive case, the energy grows linearly with particle number, consistent with extensive behavior. This confirms the stability of the gas state and supports the thermodynamic analysis above.

In contrast, the attractive regime exhibits markedly different behavior. As seen in both panels, the energy per particle continues to decrease without signs of saturation:

$$\frac{E(N)}{N} \to -\infty, \tag{5.3}$$

and no thermodynamic limit is reached. This behavior is characteristic of collapse: particles bunch together into the periodic minima of the interaction potential, and the interaction energy dominates. In the large-N limit, the particles are highly localized in the vicinity of the minima, and the ground-state energy approaches the zero temperature energy of a classical system, given by

$$E_{\text{int}}^{\text{clas}}(N) = -|V_0|\frac{N(N-1)}{2}. \tag{5.4}$$

Nonetheless, the total energy remains less negative than this pure interaction scaling, indicating that kinetic energy still plays a non-negligible role in moderating the collapse. While in a classical system at zero temperature, the particles freeze in the minimum of the potential energy, a quantum system cannot do that due to the Heisenberg uncertainty principle. Quantum fluctuations lead to a finite kinetic energy and an additional increase of the potential energy. The first correction due to the quantum fluctuations can be approximated by the ground-state energy of a harmonic oscillator:

$$E = -|V_0|\frac{N(N-1)}{2} + N\frac{\hbar\omega_0}{2} + ..., \tag{5.5}$$

where the level spacing ω_0 is obtained by the harmonic approximation of the minimum of the interaction potential:

$$V_0 \cos^2\left(\frac{2\pi}{\lambda}x\right) = V_0\left(\frac{2\pi}{\lambda}\right)^2\left(x - \frac{\lambda}{4}\right)^2 \approx \frac{1}{2}m\omega_0^2\left(x - \frac{\lambda}{4}\right)^2. \tag{5.6}$$

This correction is shown in Fig. 3 (b) as the orange dashed line. We observe a slight improvement, as the resulting energy is lower than the previous approximation. However, higher-order corrections should be considered, since the behavior is still not fully captured.

Together, the results in Fig. 3 (a)–(b) highlight a clear contrast: the repulsive regime remains stable and extensive, while the attractive regime exhibits super-extensive scaling and collapse. This behavior is a direct consequence of the all-to-all character of the cavity-mediated interaction potential.

These results pave the way for investigating more realistic systems. We introduce contact interaction and fermionic statistics and examine the effects of cavity-mediated interaction on these systems' structure.

6 Effects of Short-Range Interactions on Cavity-Mediated Systems

To study the effects of cavity-mediated long-range interactions, we explore quantum many-body systems incorporating either short-range contact interactions or fermionic statistics. Using Variational Monte Carlo (VMC), we calculate observables such as the ground-state energy, density profiles, pair correlation functions, and the static structure factor. These quantities allow us to characterize how the interplay between short-range and cavity-mediated long-range interactions modifies the system's physical behavior and stability.

To establish benchmarks, we consider two well-understood limits in the absence of cavity-mediated interactions: a weakly interacting Bose gas with short-range repulsion and an

ideal Fermi gas governed solely by quantum statistics. The weakly interacting Bose gas is accurately described by the Lieb–Liniger model, whose exact solution through the Bethe ansatz provides access to ground-state energies and correlations at all interaction strengths.
Properties of a Bose system in the absence of long-range interactions are governed by the dimensionless Lieb–Liniger parameter $\gamma = \frac{2}{\rho_0 |a_{1D}|}$, where $\rho_0 = N/L$ denotes the average particle density. The parameter γ controls the crossover from weak ($\gamma \ll 1$) to strong repulsion ($\gamma \gg 1$): the former corresponds to the Gross–Pitaevskii regime, while the latter approaches the Tonks–Girardeau limit of impenetrable bosons. Our simulations focus on a weakly interacting regime with a coupling strength $g = -\lambda/a_{1D} = 1.0$, corresponding to $\gamma = 2$ at unit density ($\rho_0 = 1\lambda^{-1}$).
On the other hand, the ideal Fermi gas represents the non-interacting limit of a fermionic system, where the Pauli exclusion principle effectively acts as repulsive interaction. At low energies, both bosonic and fermionic systems are encompassed by the universal framework of Luttinger liquid theory [Hal81; Caz+11; Caz04], which captures common properties such as phononic excitations and algebraically decaying correlations, but with different Luttinger parameters.
By comparing these well-established cases with our full model, where both short-range and cavity-mediated infinite-range interactions are present, we gain insight into how the periodic long-range potential alters fundamental properties such as the superfluid response, and the structure factor. This comparative analysis helps us interpret deviations from ideal behavior in terms of emergent correlations and the competition between interaction scales, providing a deeper understanding of the stability and phases of cavity-mediated quantum systems.

6.1 Density Profile and Frustrated Ordering

We begin by analyzing the density profiles $n(x)$ and two-body correlation functions $g^{(2)}(x_1, x_2)$ in the presence of short-range repulsion, either from contact interaction or Fermi statistics. In the repulsive regime ($V_0 > 0$), both the cavity-mediated and short-range interactions discourage particles from occupying nearby positions. As expected, the density profiles remain relatively flat, with weak periodic modulations slightly softened by repulsion.
In Fig. 4 we show the density profile both for a system with contact interaction and a fermionic system. It is quite remarkable to see how, in the fermionic case, the behavior of the density profile is not as directly analogous to the purely long-range interaction case as it is for the contact interaction case. Although both fermions and the cavity-mediated interaction introduce a repulsive type of constraint, there is a competition: the system tends to behave more gas-like and lose the periodicity enforced by the cavity potential. This effect is more pronounced in the attractive regime (discussed further below), but it arises from the same fundamental mechanism.
For instance, when $V_0 = -10\varepsilon$, the cavity-mediated interaction becomes less dominant as the particle number increases, allowing the fermionic repulsion to push the system toward a Fermi-gas-like configuration, though still retaining some imprint of the periodic potential. In the bosonic case with contact interaction, a similar effect could arise; however, the contact repulsion is much weaker than the cavity interaction, so the system behaves nearly identically to the ideal Bose gas with only long-range interactions.
The situation becomes more interesting in the attractive regime ($V_0 < 0$), where the cavity-mediated interaction tends to localize particles in its potential minima, while short-range repulsion resists clustering. This competition creates frustration between the two interactions.
It is worth emphasizing that frustration only emerges in the many-body setting, and under our assumed system size $L = 2\lambda$. For two particles in this setup, Pauli exclusion enforces separation, while the cavity-mediated interaction favors configurations where particles occupy

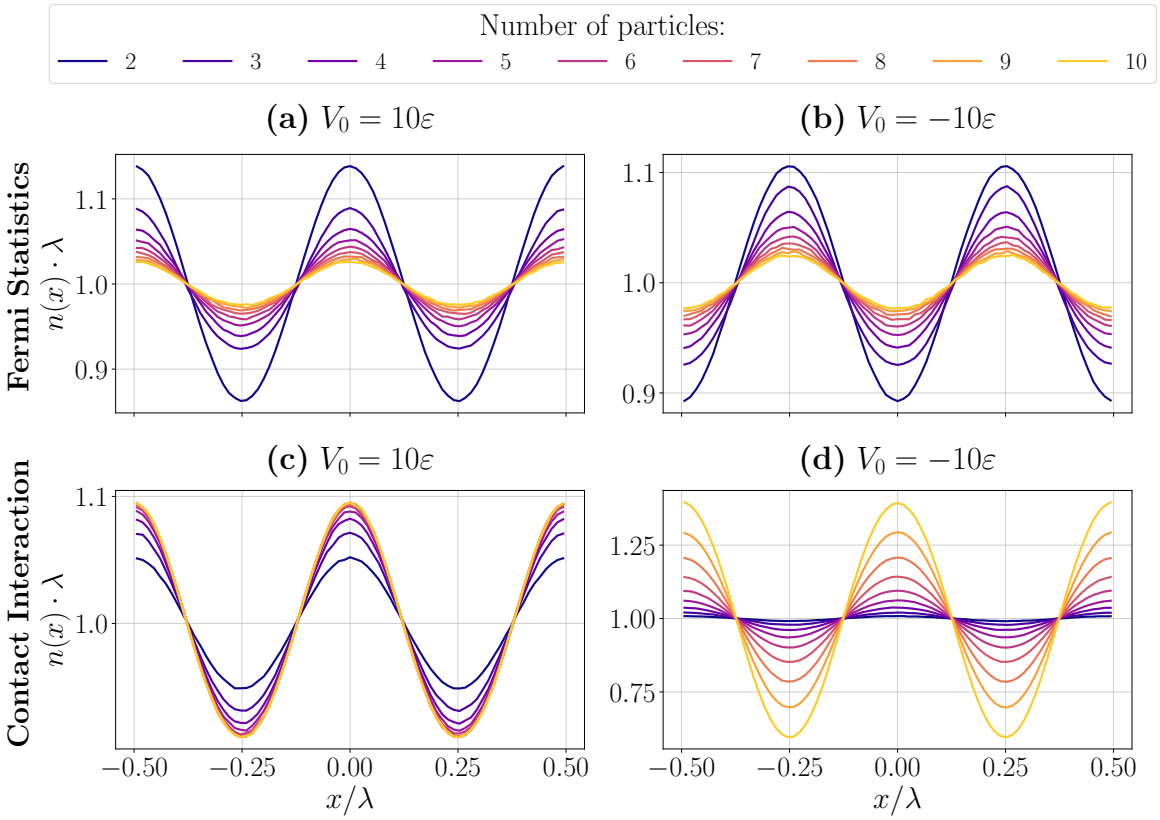

Figure 4: Density profiles in the presence of short-range correlations for particle numbers $N = 2, \ldots, 10$ Panel (a): Fermionic system with repulsive long-range interaction ($V_0 > 0$). Panel (b): Fermionic system with attractive long-range interaction ($V_0 < 0$). Panel (c): Bosonic system with contact interaction $\gamma > 0$ and repulsive long-range interaction. Panel (d): Bosonic system with contact interaction and attractive long-range interaction. All simulations are performed by fixing the length of the system $L = 2\lambda$ and changing th density $\rho = N/L$.

the minima of the interaction potential. In this particular case, both conditions can be satisfied when the particles are separated by one period of the interaction lattice, so the system does not experience frustration. However, this absence of frustration is not general: for smaller systems, for example, $L = \lambda$, even the two-particle case becomes frustrated, as the particles can no longer remain one period apart. In larger systems, on the other hand, frustration only arises at higher particle numbers, since the increased space allows more freedom in satisfying interaction constraints. The onset of frustration therefore depends not only on the number of particles but also on the system size, which together determine whether all pairwise constraints can be simultaneously accommodated.

To explore this effect in detail, we focus on the fermionic system with $N = 5$ particles—a size large enough to exhibit spatial structure, but small enough to resolve individual correlations. We choose the fermionic case because the effects of frustration are visually more pronounced due to the strong Pauli repulsion. Similar effects are also present in bosonic systems with contact interactions, though they are significantly weaker and harder to visualize with the same clarity.

Figure 5 shows both the density profile and the two-body correlation function for increasing attractive strength. Panel (a) reveals that for moderate attraction ($1 < |V_0|/\varepsilon < 20$), the density remains nearly uniform, though faint modulations emerge due to the underlying cavity-mediated interaction.

This effect becomes even clearer when observing the two-body correlation function $g^{(2)}(x_1, x_2)$

in Fig. 5 (b). At $V_0 = -10\varepsilon$, which corresponds to an intermediate attraction, the pair distribution presents a very uniform pattern, but with a faint periodic modulation that has maxima now at the zeros of the interaction instead of the minima, corresponding to a half-period phase shift in the density profile, see Fig. 5 (a). The system avoids both the interaction maxima and the diagonal $x_1 = x_2$, which is forbidden by Fermi statistics.

This results in a frustrated arrangement that balances both types of interaction: the attractive cavity-mediated potential, which favors clustering, and the Pauli exclusion principle, which prevents particle overlap. As a result, the particles tend to organize near the zeros of the interaction potential, reflecting a nontrivial compromise between these opposing tendencies.

As $|V_0|$ increases further, the periodic structure imposed by the cavity-mediated interaction begins to dominate. The system crystallizes into density maxima that align with the minima of the interaction potential, similar to what is observed in the long-range-only case. However, even in this limit, the system continues to avoid the diagonal in $g^{(2)}$, preserving Pauli exclusion. The width of this forbidden region narrows as the attraction grows stronger, reflecting increased localization around the cavity minima and the growing dominance of the cavity-mediated interaction, Fig. 5 (a) and (c) for $V_0 < -30\varepsilon$, where the peak positions match those of the long-range-only case.

This frustrated regime, where particles are caught between the ordering tendency of the long-range interaction and the repulsive constraint imposed by Fermi statistics, defines a nontrivial configuration—neither an ideal Fermi gas nor the delocalized bound state found in the purely long-range Bose case. To quantify and further characterize the transition out of this regime, we compute both the energy per particle E/N and the Leggett upper bound for the superfluid fraction as functions of interaction strength.

The superfluid fraction is expected to remain finite as long as the system retains a delocalized, fluid-like character, and to drop rapidly to zero once the particles begin to localize within the cavity minima. This makes it a useful indicator of the crossover between the frustrated regime and the interaction-dominated, symmetry-broken state.

As shown in Fig. 5 (d)–(e), the superfluid response remains large in the frustrated regime and becomes strongly suppressed once the long-range attraction becomes dominant. This crossover occurs just before the energy per particle turns negative, signaling the onset of a many-body-bound state.

It is important to point out that the gas-like phase for attractive interactions is a mesoscopic one, that is it exists only for a finite number of particles and vanishes in the thermodynamic limit. By increasing the number of particles, the system enters the delocalized bound state identified in the long-range-only case and gradually loses all superfluid response, as reflected by the vanishing Leggett bound.

6.2 Energy Scaling and Qualitative Phase Diagram

We now extend the energy analysis to systems that include additional short-range repulsion, either through Fermi statistics or weak contact interaction.

For strong long-range interactions, the observed behavior closely resembles that of the purely long-range case. In the repulsive regime, $V_0 > 0$, the energy per particle E/N converges with increasing N, confirming the existence of a well-defined thermodynamic limit. In the attractive regime, $V_0 < 0$, the energy decreases with N and shows signs of collapse, although the rate of divergence is reduced due to the presence of repulsive effects.

The most notable difference is found at $V_0 = 0$, where the energy is no longer zero but reflects the baseline contribution from the short-range terms. In the fermionic case, this corresponds to the energy of the ideal Fermi gas, which is significantly higher. In the bosonic case with contact interaction, the shift is much smaller, consistent with the weaker repulsion.

Importantly, the short-range repulsion acts to delay the onset of collapse. This stabilization is especially visible in the fermionic case, where Pauli repulsion remains strong even as V_0 becomes increasingly negative. For bosons with contact interaction, the effect is much weaker and only noticeable at small N. As such, while the overall instability of the attractive regime persists, its onset is significantly modified by the nature and strength of short-range repulsion.
In the previous section, we identified the emergence of a frustrated regime when contact interactions are introduced and the system satisfies $E/N > 0$. We observed that the transition between different regimes occurs at the point where $E/N \approx 0$, which allowed us to determine the zero-crossings of the energy curves shown in Fig. 6 (a)–(b). Based on this criterion, Fig. 6 (c) presents a qualitative phase diagram constructed by identifying the values of V_0 at which $E/N = 0$, which we interpret as indicative of a change in the system's behavior.
This phase diagram reveals three distinct regimes. In the repulsive case ($V_0 > 0$), the system remains gas-like across all interaction strengths, exhibiting only a weak periodic modulation induced by the LR interaction. In the attractive regime ($V_0 < 0$), two qualitatively different phases emerge. For small values of V_0, the system remains in a mesoscopic gas phase: the LR attraction is not sufficiently strong to induce localization in the minima of the interaction potential, and the particles remain delocalized, exhibiting gas-like behavior. However, beyond a certain critical value of V_0, which depends on the particle number, the system localizes in the minima of the interaction potential, forming what we define as a delocalized bound state. We also observe that, in the presence of contact interactions, the critical amplitude V_0 required for localization is lower than in the fermionic case. This difference can be attributed to the weaker effective repulsion between bosons with contact interactions, making the system more susceptible to clustering under attractive LR forces.

6.3 Structure Factor and Low-Momentum Excitations

The static structure factor $S(k)$ quantifies the correlations in momentum space and can be used to extract information on the low-energy excitations. In particular, the Feynman relation [Fey54],

$$\epsilon(k) \approx \frac{\hbar^2 k^2}{2mS(k)}, \tag{6.1}$$

defines the energy of the excitation $\epsilon(k)$, under the assumption that for a given momentum k, all excitations have the same energy. In other words, the Feynman relation works well for collective excitations such as phonons, which have a linear dispersion relation $\epsilon(k) = \hbar|k|c$ for small momenta $k \to 0$. In addition, peaks and dips present in $S(k)$ at finite momenta would indicate enhanced or suppressed density fluctuations, often reflecting the underlying interaction potential or emergent spatial order.
Figure 7 reports the structure factor. We discuss first the case of long-range interactions, Fig. 7 (a) and (d). For attractive interactions (Fig. 7 (a)), we observe pronounced peaks at multiples of the cavity modulation wavevector, reflecting the spatial periodicity imposed by the interaction. For attractive LR interactions, high peaks in $S(k)$ remain if contact interactions (Fig. 7 (b)) or Fermi statistics (Fig. 7 (c)) are considered. This indicates that the system has density modulations at these wavelengths, consistent with the formation of clustered structures aligned with the cavity potential. In contrast, the repulsive case (bottom row in Fig. 7) shows a very pronounced dip at $k = 2\pi/\lambda$, corresponding to the first cavity wavevector. These dips signal that the system strongly suppresses density fluctuations at the cavity wavelength, effectively resisting the spatial ordering imposed by the interaction potential. Physically, this means that the repulsive cavity-mediated interaction penalizes density modulations at its characteristic wavelength, favoring instead a more uniform gas-like struc-

ture. However, at low momentum, independently of the sign of cavity-induced interactions $S(k)$ remains flat, indicating the absence of phonons. This implies that the system lacks collective long-range excitations and therefore cannot be described as a superfluid or Luttinger liquid in this regime; instead, it resembles the behavior of an ideal Bose gas.
Thus, it is instructive to study $S(k)$ in a system with finite compressibility, such as a Bose gas with contact interaction, Fig. 7 (b) and (e), or a Fermi gas, Fig. 7 (c) and (f). In both cases, the structure factor acquires a linear behavior at small k, which indicates the emergence of phonon-like collective excitations, so that the long-range properties can be described by the Luttinger liquid theory. Within this theory, the Luttinger parameter $K = v_F/v_s$ defined by the ratio between the speed of sound v_s and Fermi velocity $v_F = \hbar\pi\rho/m$, is a central quantity that characterizes the low-energy properties of compressible 1D fluids. Its value governs the decay of correlation functions, with larger values of K indicating enhanced coherence. The specific value of the Luttinger parameter can be extracted from the equation of state, which for a gas with contact interactions was obtained using the Bethe ansatz by Lieb and Liniger [LL63]. We use $|a_{1D}| = 1\,\lambda$ and $\rho = 1\,\lambda^{-1}$ so that the Lieb-Liniger parameter is $\gamma = 2/(\rho|a_{1D}|) = 2$ and Bethe *ansatz* theory predicts $K = 2.5235...$ [Caz04] for the Luttinger parameter. For an ideal Fermi gas, the speed of sound coincides with the Fermi velocity and $K = 1$. Thus, the slope of the linear part in $S(k)$ is proportional to the Luttinger parameter,

$$S(k) \approx \frac{\hbar|k|}{2mv_s} = \frac{K}{2\pi\rho}k, \tag{6.2}$$

as shown with the red dashed lines in Fig. 7. We find a close agreement in the case of repulsive cavity-induced interactions, see Fig. 7 (e) and (f). The small discrepancy should be attributed to the approximate variational wavefunction, as in the absence of LR interactions, we find the same small difference in the slope (see Appx. G for more details). This close agreement also suggests that the cavity-mediated interactions do not significantly modify the phononic excitations of the system in the repulsive regime. Its primary impact lies in the intermediate- and short-range correlations, while the low-energy Luttinger liquid behavior remains essentially intact. Contrarily, the low-momentum part gets affected by the attractive LR interactions (Fig. 7 (b) and (c)), in this case, the structure factor changes its slope as the strength of the attractive cavity interaction increases. This suggests that the sound velocity depends on the total particle number, highlighting how the presence of long-range attraction disrupts extensivity and modifies the collective response of the system. The speed of sound v_s grows as the number of particles is increased, pointing to the formation of regions of a large local density as the system enters a collapsing regime.

7 Conclusions and Outlook

This Master's Thesis studies the ground-state properties of a one-dimensional quantum system with cavity-mediated long-range interactions in continuous space, using numerical methods across different interaction regimes and quantum statistics. Although the one-dimensional setup might seem simple, the system displays a rich variety of behaviors as summarized in the phase diagram.
We investigate the many-body properties in the absence of short-range interactions, isolating the effects of cavity-mediated long-range potentials. Such a system exhibits two qualitatively different regimes depending on the sign of the interaction strength. For attractive interactions, particles strongly cluster at the periodic minima of the potential, leading to pronounced density modulations, a vanishing superfluid fraction, and the absence of a well-defined thermodynamic limit, we refer to this regime as a delocalized bound state. In contrast, repulsive long-range interactions produce a delocalized phase characterized by weak periodic density

modulations, finite superfluid fraction, and a well-defined thermodynamic limit. Notably, the pure system lacks conventional phononic excitations, as evidenced by the flat low-momentum behavior of the static structure factor, indicating an unconventional excitation spectrum in the purely cavity-mediated regime.

The incorporation of short-range repulsion, through either contact interactions or fermionic statistics, significantly modifies the system's properties. In the repulsive interaction regime, short-range repulsion restores phononic excitations, as evidenced by the linear low-momentum dependence of the static structure factor, allowing one to make use of the Luttinger liquid theory. The cavity-mediated interactions only weakly perturb the low-energy excitations in this regime. Instead, the interplay between long-range attraction and short-range repulsion generates a frustrated mesoscopic phase marked by intricate spatial correlations and a finite superfluid fraction. As attraction is increased further, the system undergoes a transition into a delocalized bound state phase, reflecting a rich competition between the repulsive forces and clustering tendencies.

From a methodological point, we developed a many-body trial wavefunction based on the exact two-body solution of the cavity-mediated potential. This wavefunction was implemented within both Variational Monte Carlo (VMC) and Diffusion Monte Carlo (DMC) methods. We validated these methods by benchmarking against known analytical limits (perturbative expansions), exactly solvable cases (ideal Fermi gas, Bethe ansatz for Lieb-Liniger gas) and alternative methods (imaginary-time propagation for two-particle case), ensuring consistency across different interaction regimes. Additionally, convergence tests were performed with respect to simulation parameters such as particle number, time step size, and projection time, confirming the robustness and accuracy of our approach. These validations guarantee reliable quantitative predictions for ground-state energies and correlation functions in cavity-mediated many-body systems. The numerical methods developed here are versatile and extendable to higher-dimensional or more realistic cavity-QED models.

In conclusion, this Master's Thesis combines a physically motivated model with flexible numerical tools to explore a range of rich many-body phenomena. It offers both a foundation for future simulations and concrete insight into the behavior of ultracold atoms coupled to cavity fields.

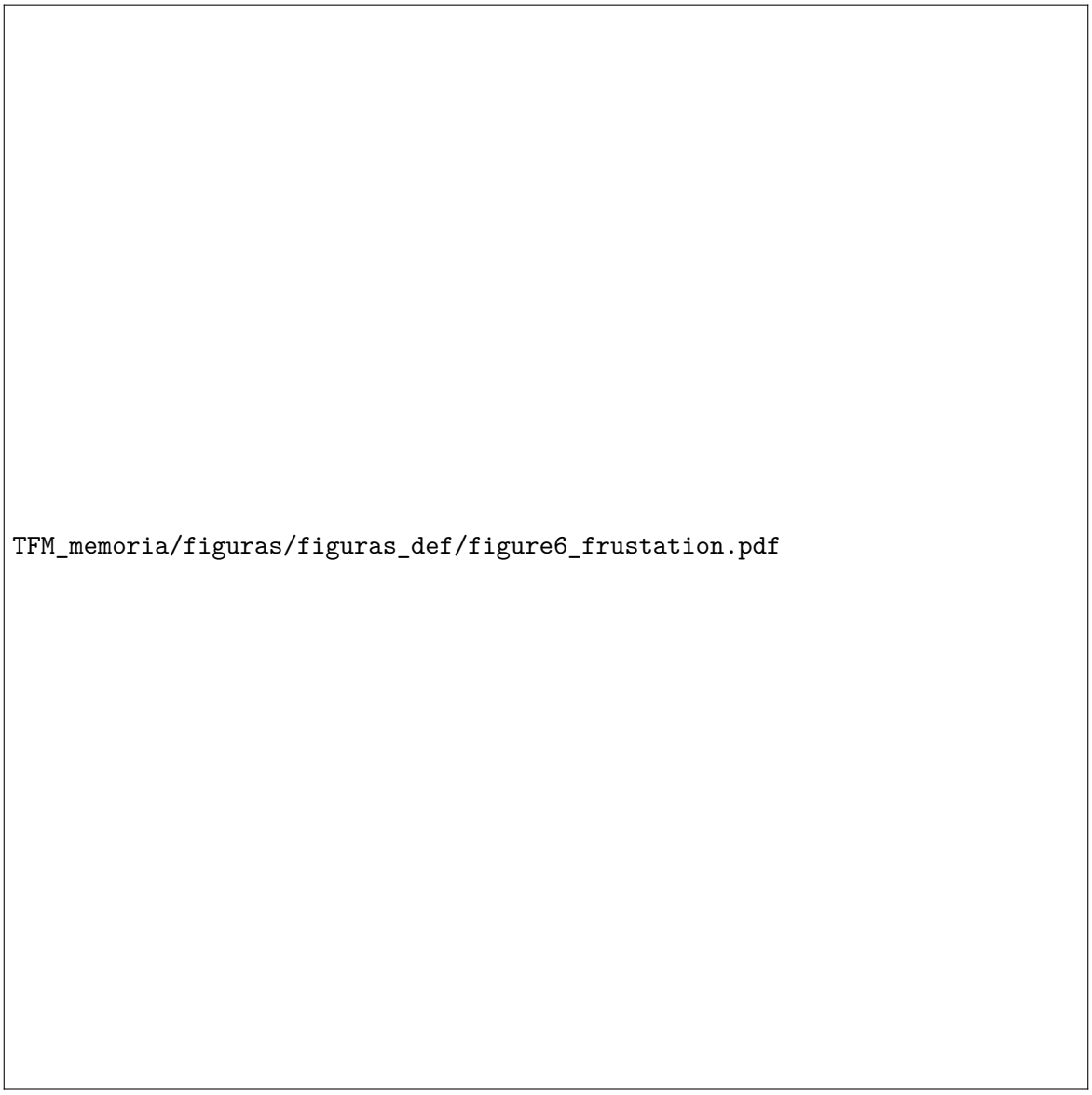

Figure 5: Results for a spinless fermionic system with $N = 5$ particles and attractive cavity-mediated interactions. Panel (a): Density profile $n(x)$ for varying V_0, exhibiting a shift at weak coupling and recovering the bosonic periodic structure at strong coupling. Panels (b)–(c): Two-body correlation function $g^{(2)}(x_1, x_2)$ for $V_0 = -10.0\,\varepsilon$ and $V_0 = -30.0\,\varepsilon$, respectively. Panel (d): Energy per particle E/N as a function of V_0, showing a zero crossing. Panel (e): Superfluid fraction obtained from the Leggett bound, Eq. (3.16), indicating a crossover in the superfluid response. All simulations are performed by fixing the system size $L = 2\lambda$ and changing the density $\rho = N/L$.

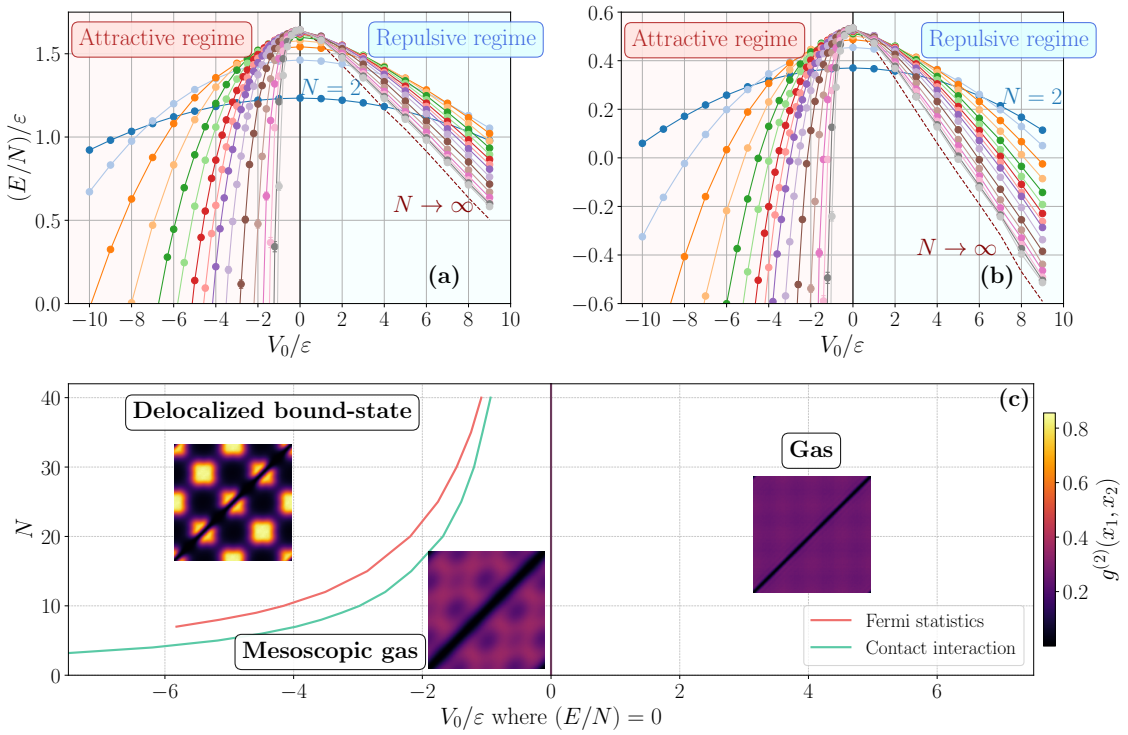

Figure 6: Ground-state energy of bosons interacting via both the cavity-mediated long-range potential and short-range interactions. Symbols show VMC results. Panel (a): Fermionic system. Panel (b): Bosonic system with weak contact interaction. In the repulsive regime ($V_0 > 0$), an extrapolated thermodynamic limit is shown as the dashed maroon line. Panel (c): Qualitative phase diagram, distinguishing three regimes: delocalized bound state, mesoscopic gas, and gas phase. The mesoscopic gas is separated by a vertical $V_0 = 0$ line with the thermodynamically stable gas phase and by $E/N = 0$ line with the delocalized bound state phase. Three characteristic representative pair correlation functions are shown to illustrate the change in spatial correlations across these regimes. All simulations are performed at fixed density $\rho = 1/\lambda$, varying the system size as $L = N/\rho$, except for the pair correlation functions $g^{(2)}(x_1, x_2)$ in panel (c), which are computed at fixed length $L = 2\lambda$ for better visualization.

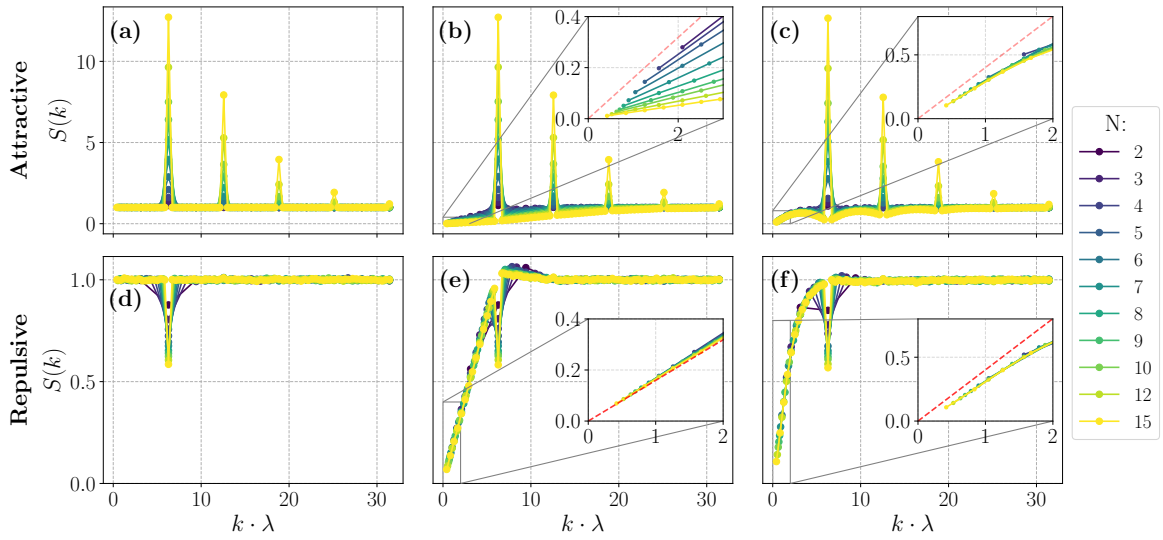

Figure 7: Static structure factor $S(k)$ calculated for various particle numbers N at constant density $\rho = 1/\lambda$ for attractive (upper row) or repulsive (bottom row) long-range interactions. Panel (a) and (d): Bosonic system with only long-range interactions, attractive in (a) and repulsive in (d). Panel (b) and (e): Fermionic system with long-range interactions, attractive in (b) and repulsive in (e). Dashed lines indicate the theoretical prediction for non-interacting fermions. Panel (c) and (f): Bosonic system with both short- and long-range interactions, attractive in (c) and repulsive in (f). Dashed lines indicate the Luttinger liquid prediction with interaction parameter $\gamma = 2$ and Luttinger parameter $K = 2.5235...$

References

[Bar+12] M. A. Baranov, M. Dalmonte, et al. "Condensed Matter Theory of Dipolar Quantum Gases". In: *Chemical Reviews* 112.9 (2012), pp. 5012–5061. DOI: 10.1021/cr2003568.

[BCV03] A. T. Black, H. W. Chan, and V. Vuletić. "Observation of Collective Friction Forces due to Spatial Self-Organization of Atoms: From Rayleigh to Bragg Scattering". In: *Physical Review Letters* 91.20 (2003), p. 203001. DOI: 10.1103/PhysRevLett.91.203001.

[BP12] M. Boninsegni and N. V. Prokof'ev. "Colloquium: Supersolids: What and where are they?" In: *Reviews of Modern Physics* 84 (2012), pp. 759–776. DOI: 10.1103/RevModPhys.84.759.

[Caz+11] M. A. Cazalilla, R. Citro, et al. "One dimensional bosons: From condensed matter systems to ultracold gases". In: *Reviews of Modern Physics* 83.4 (2011), pp. 1405–1466. DOI: 10.1103/RevModPhys.83.1405.

[Caz04] M. A. Cazalilla. "Bosonizing one-dimensional cold atomic gases". In: *Journal of Physics B: Atomic, Molecular and Optical Physics* 37.7 (2004), S1. DOI: 10.1088/0953-4075/37/7/051.

[Dog+16] N. Dogra, F. Brennecke, et al. "Phase transitions in a Bose-Hubbard model with cavity-mediated global-range interactions". In: *Physical Review A* 94 (2016), p. 023632. DOI: 10.1103/PhysRevA.94.023632.

[Dom] M. Dominguez-Navarro. *Quantum Monte Carlo study of systems interacting via long-range interactions mediated by a cavity (TFM–2025)*. https://github.com/martadomin/Cavity_mediated_interaction_TFM. Accessed: 2025-07-06.

[Fey54] R. P. Feynman. "Atomic Theory of the Two-Fluid Model of Liquid Helium". In: *Physical Review* 94 (2 1954), pp. 262–277. DOI: 10.1103/PhysRev.94.262.

[FHS10] R. P. Feynman, A. R. Hibbs, and D. F. Styer. *Quantum Mechanics and Path Integrals*. Emended. Mineola, NY: Dover Publications, 2010.

[FP89] H. Flyvbjerg and H. G. Petersen. "Error estimates on averages of correlated data". In: *The Journal of Chemical Physics* 91.1 (1989), pp. 461–466. DOI: 10.1063/1.457480.

[GB17] C. Gross and I. Bloch. "Quantum simulations with ultracold atoms in optical lattices". In: *Science* 357.6355 (2017), pp. 995–1001. DOI: 10.1126/science.aal3837.

[GLG10] S. Gopalakrishnan, B. L. Lev, and P. M. Goldbart. "Atom-light crystallization of Bose-Einstein condensates in multimode cavities: Nonequilibrium classical and quantum phase transitions, emergent lattices, supersolidity, and frustration". In: *Phys. Rev. A* 82 (4 2010), p. 043612. DOI: 10.1103/PhysRevA.82.043612.

[Gre+02] M. Greiner, O. Mandel, et al. "Quantum phase transition from a superfluid to a Mott insulator in a gas of ultracold atoms". In: *Nature* 415.6867 (2002), pp. 39–44. DOI: 10.1038/415039a.

[Gui21] G. Guijarro. "Quantum Monte Carlo Study of Few- and Many-Body Bose Systems in One and Two Dimensions". Available at https://arxiv.org/abs/2012.14545. PhD thesis. Universitat Politècnica de Catalunya (UPC), 2021.

[Hal81] F. D. M. Haldane. "'Luttinger liquid theory' of one-dimensional quantum fluids. I. Properties of the Luttinger model and their extension to the general 1D interacting spinless Fermi gas". In: *Journal of Physics C: Solid State Physics* 14.19 (1981), p. 2585. DOI: 10.1088/0022-3719/14/19/010.

[Jak+98] D. Jaksch, C. Bruder, et al. “Cold Bosonic Atoms in Optical Lattices”. In: *Phys. Rev. Lett.* 81 (15 1998), pp. 3108–3111. DOI: 10.1103/PhysRevLett.81.3108.

[JC63] E. T. Jaynes and F. W. Cummings. “Comparison of quantum and semiclassical radiation theories with application to the beam maser”. In: *Proceedings of the IEEE* 51.1 (1963), pp. 89–109. DOI: 10.1109/PROC.1963.1664.

[KFS96] I. Kosztin, B. Faber, and K. Schulten. “Introduction to the Diffusion Monte Carlo Method”. In: *American Journal of Physics* 64.5 (1996), pp. 633–644. DOI: 10.1119/1.18168.

[Kli+15] J. Klinder, H. Keßler, et al. “Dynamical phase transition in the open Dicke model”. In: *Proceedings of the National Academy of Sciences* 112.11 (2015), pp. 3290–3295. DOI: 10.1073/pnas.1417132112.

[KP22] P. Karpov and F. Piazza. “Light-Induced Quantum Droplet Phases of Lattice Bosons in Multimode Cavities”. In: *Physical Review Letters* 128.10 (2022), p. 103201. DOI: 10.1103/PhysRevLett.128.103201.

[Lah+09] T. Lahaye, C. Menotti, et al. “The physics of dipolar bosonic quantum gases”. In: *Reports on Progress in Physics* 72.12 (2009), p. 126401. DOI: 10.1088/0034-4885/72/12/126401.

[Lan+16] R. Landig, L. Hruby, et al. “Quantum phases from competing short- and long-range interactions in an optical lattice”. In: *Nature* 532.7600 (2016), pp. 476–479. DOI: 10.1038/nature17409.

[Leg98] A. J. Leggett. “On the Superfluid Fraction of an Arbitrary Many-Body System at $T = 0$”. In: *Journal of Statistical Physics* 93.3 (1998), pp. 927–941. DOI: B:JOSS.0000033170.38619.6c.

[Lew+07] M. Lewenstein, A. Sanpera, et al. “Ultracold atomic gases in optical lattices: mimicking condensed matter physics and beyond”. In: *Advances in Physics* 56.2 (2007), pp. 243–379. DOI: 10.1080/00018730701223200.

[LL63] E. H. Lieb and W. Liniger. “Exact Analysis of an Interacting Bose Gas. I. The General Solution and the Ground State”. In: *Physical Reviews* 130 (4 1963), pp. 1605–1616. DOI: 10.1103/PhysRev.130.1605.

[MMR08] C. Maschler, I. B. Mekhov, and H. Ritsch. “Ultracold atoms in optical lattices generated by quantized light fields”. In: *The European Physical Journal D* 46.3 (2008), pp. 545–560. DOI: 10.1140/epjd/e2008-00016-4.

[Mot+12] R. Mottl, F. Brennecke, et al. “Roton-Type Mode Softening in a Quantum Gas with Cavity-Mediated Long-Range Interactions”. In: *Science* 336.6088 (2012), pp. 1570–1573. DOI: 10.1126/science.1220314.

[MR05] C. Maschler and H. Ritsch. “Cold Atom Dynamics in a Quantum Optical Lattice Potential”. In: *Physical Review Letters* 95.26 (2005), p. 260401. DOI: 10.1103/PhysRevLett.95.260401.

[Nag+10] D. Nagy, G. Kónya, et al. “Dicke-Model Phase Transition in the Quantum Motion of a Bose-Einstein Condensate in an Optical Cavity”. In: *Physical Review Letters* 104.13 (2010), p. 130401. DOI: 10.1103/PhysRevLett.104.130401.

[NSD08] D. Nagy, G. Szirmai, and P. Domokos. “Self-organization of a Bose-Einstein condensate in an optical cavity”. In: *The European Physical Journal D* 48.1 (2008), pp. 127–137. DOI: 10.1140/epjd/e2008-00074-6.

[PC04] D. Porras and J. I. Cirac. “Effective Quantum Spin Systems with Trapped Ions”. In: *Physical Review Letters* 92.20 (2004), p. 207901. DOI: 10.1103/PhysRevLett.92.207901.

[SBC02] A. Sarsa, J. Boronat, and J. Casulleras. “Quadratic Diffusion Monte Carlo and Pure Estimators for Atoms”. In: *The Journal of Chemical Physics* 116.14 (2002), pp. 5956–5962. DOI: 10.1063/1.1446847.

[TAU16] J. Toulouse, R. Assaraf, and C. J. Umrigar. “Chapter Fifteen - Introduction to the Variational and Diffusion Monte Carlo Methods”. In: *Electron Correlation in Molecules – ab initio Beyond Gaussian Quantum Chemistry*. Ed. by P. E. Hoggan and T. Ozdogan. Vol. 73. Advances in Quantum Chemistry. Academic Press, 2016, pp. 285–314. DOI: https://doi.org/10.1016/bs.aiq.2015.07.003.

[Vij+24] J. Vijayan, J. Piotrowski, et al. “Cavity-mediated long-range interactions in levitated optomechanics”. In: *Nature Physics* 20.5 (2024), pp. 859–864. DOI: 10.1038/s41567-024-02405-3.

[VJD05] A. Vukics, J. Janszky, and P. Domokos. “Cavity cooling of atoms: a quantum statistical treatment”. In: *Journal of Physics B: Atomic, Molecular and Optical Physics* 38.10 (2005), p. 1453. DOI: 10.1088/0953-4075/38/10/005.

A Theoretical Model

To obtain the effective Hamiltonian from Ref. [Mot+12], several standard approximations are employed from the theoretical derivations in Ref.[MR05; MMR08]. First, the rotating wave approximation (RWA) is applied by transforming to a frame rotating at the pump frequency ω_p, allowing rapidly oscillating terms to be neglected. Second, the dipole approximation assumes that the electric field is spatially uniform over the extent of a single atom, simplifying the interaction Hamiltonian.

The original Jaynes-Cummings model, introduced in Ref. [JC63], describes the interaction between a single two-level atom and a quantized cavity mode. In the many-body generalization used here, the two-level structure is effectively replaced by continuous atomic degrees of freedom, and the atomic population is treated using bosonic field operators.

In the specific experimental realization of Ref. [Mot+12], this general framework has several modifications. Notably, while the original model includes both a transverse classical pump and also a direct laser in the direction of the cavity that directly populates the cavity mode, the experiment uses only a transverse laser. In this case, the cavity mode is populated exclusively via photon scattering by the atoms, and thus, the coherent cavity drive term is absent. Moreover, the transverse laser is far-detuned from the atomic transition so that the electronically excited state is only virtually populated. This allows for its adiabatic elimination, leaving an effective model involving only ground-state atoms.

The total Hamiltonian of the system is composed of three contributions: the atomic, the cavity field, and the atom-cavity interaction.

Atomic part: The atomic Hamiltonian is given by

$$\hat{H}_A = \int d^3\mathbf{r}\hat{\Psi}^\dagger(\mathbf{r}) \left[\frac{\mathbf{p}^2}{2m} + V_p \cos^2(k_L z) + \frac{g}{2} c\hat{\Psi}(\mathbf{r}) \right] \hat{\Psi}(\mathbf{r}), \tag{A.1}$$

where $\hat{\Psi}(\mathbf{r})$ is the atomic field operator, and $\hat{a}$ and $\hat{a}^\dagger$ are the photon annihilation and creation operators associated with the cavity mode. The first term represents the kinetic energy of the atoms, the second corresponds to a static optical lattice potential of depth V_p along the z-axis, and the third describes contact interactions between atoms. The interaction strength is given by $g = 4\pi\hbar^2 a/m$, where a is the s-wave scattering length and m is the atomic mass.

Cavity part: The energy of the quantized cavity field is

$$\hat{H}_C = -\hbar\Delta_c \hat{a}^\dagger \hat{a}, \tag{A.2}$$

where $\Delta_c = \omega_p - \omega_c$ is the detuning between the pump frequency and the cavity resonance.

Atom-cavity interaction: The interaction between atoms and the cavity mode takes the form

$$\hat{H}_{A-C} = \int d^3\mathbf{r}\, \hat{\Psi}^\dagger(\mathbf{r}) \left[\hbar\eta \cos(k_L x)\cos(k_L z) \left(\hat{a} + \hat{a}^\dagger \right) + \hbar U_0 \cos^2(k_L x) \hat{a}^\dagger \hat{a} \right] \hat{\Psi}(\mathbf{r}), \tag{A.3}$$

where the first term describes the scattering of photons from the pump laser into and out of the cavity mode. The parameter η is the two-photon Rabi frequency, resulting from a virtual process in which an atom absorbs a pump photon and emits it into the cavity mode. The second term describes how each atom, depending on its position within the cavity field, shifts the cavity resonance frequency by an amount proportional to U_0 for each photon present. Here, U_0 quantifies how strongly a single maximally coupled atom perturbs the cavity frequency in the far-detuned regime.

To further simplify the description, one assumes that the cavity field reaches its steady state on a timescale faster than the atomic motion. This allows us to solve the full Heisenberg

equation of motion for the cavity field operator

$$\frac{\partial \hat{a}}{\partial t} = \left\{ i \left[\Delta_c - i\eta \int d^3\mathbf{r}, \hat{\Psi}^\dagger(\mathbf{r}) \cos^2(k_L x) \hat{\Psi}(\mathbf{r}) \right] - k_L \right\} \hat{a} - iU_0 \int d^3\mathbf{r}, \hat{\Psi}^\dagger(\mathbf{r}) \cos(k_L x) \cos(k_L z) \hat{\Psi}(\mathbf{r}), \tag{A.4}$$

and using the steady-state assumption, $\partial \hat{a}/\partial t = 0$, and defining the order parameter $\hat{\Theta}$ and the bunching parameter $\hat{\mathcal{B}}$

$$\hat{\Theta} = \int d^3\mathbf{r} \hat{\Psi}^\dagger(\mathbf{r}) \cos(k_L x) \cos(k_L z) \hat{\Psi}(\mathbf{r}) \qquad \hat{\mathcal{B}} = \int d^3\mathbf{r} \hat{\Psi}^\dagger(\mathbf{r}) \cos^2(k_L x) \hat{\Psi}(\mathbf{r}),$$

one obtains the steady-state solution

$$\hat{a} = \frac{\eta \hat{\Theta}}{\Delta_c - U_0 \hat{\mathcal{B}} + i\kappa}. \tag{A.5}$$

Here, $\hat{\Theta}$ quantifies the degree of atomic density modulation matching the interference pattern between pump and cavity fields, it acts as an order parameter for the self-organization transition, and $\hat{\mathcal{B}}$ measures the overlap between the atomic density and the cavity mode, higher values indicate stronger spatial localization within the cavity mode structure.
Substituting Eq. (A.5) into the full Hamiltonian yields an effective two-body interaction term mediated by the cavity field:

$$\hat{H}_{\text{eff}} = \hat{H}_A + V_0 \int d^3\mathbf{r}\, d^3\mathbf{r}'\, \hat{\Psi}^\dagger(\mathbf{r}) \hat{\Psi}^\dagger(\mathbf{r}') \hat{\Psi}(\mathbf{r}) \cos(k_L x) \cos(k_L z) \cos(k_L x') \cos(k_L z') \hat{\Psi}(\mathbf{r}'), \tag{A.6}$$

where the effective interaction strength is given by

$$V_0 = \hbar \frac{\eta^2}{\Delta_c - U_0 \mathcal{B}_0}, \tag{A.7}$$

assuming the effective detuning satisfies $(\Delta_c - U_0 \mathcal{B}_0) \gg \kappa$, so that the imaginary part of the denominator in Eq. (A.5) can be neglected. Here, $\mathcal{B}_0 = \langle \hat{\mathcal{B}} \rangle$ is the mean value of the bunching parameter in the steady state.

B Imaginary Time Evolution and Quantum Monte Carlo

In this section, we present the technical details of the numerical methods used to study and characterize the ground-state properties of the one-dimensional Bose gas with cavity-mediated long-range interactions described in Section 2. We begin with the imaginary time evolution (ITE) technique, which provides a general route to obtain the ground-state wavefunction for systems with few particles. We then introduce two stochastic Quantum Monte Carlo methods—Variational Monte Carlo (VMC) and Diffusion Monte Carlo (DMC)—which allow us to access larger many-body systems where exact diagonalization and direct evolution become computationally intractable.
In order to validate some of the proposed methods, we performed a series of benchmark tests, presented in the next section, Sec. C.

B.1 Imaginary Time Evolution

In systems where neither an analytical solution nor a suitable variational ansatz is available, numerical methods must be used to obtain the ground-state wavefunction. Imaginary Time Evolution (ITE) is one of them. This method is based on the imaginary-time formulation.

To derive the imaginary-time formulation, we perform a change of variables in the time-dependent Schrödinger equation by introducing $\tau = \frac{it}{\hbar}$. This transforms the original equation

$$i\hbar \frac{\partial \Psi(\mathbf{R}, t)}{\partial t} = \left[-\frac{\hbar^2}{2m} \nabla^2_{\mathbf{R}} + V(\mathbf{R}) \right] \Psi(\mathbf{R}, t), \tag{B.1}$$

into the imaginary-time version,

$$-\frac{\partial \Psi(\mathbf{R}, \tau)}{\partial \tau} = \left[-\frac{\hbar^2}{2m} \nabla^2_{\mathbf{R}} + V(\mathbf{R}) \right] \Psi(\mathbf{R}, \tau). \tag{B.2}$$

The general solution of this equation can be written as an expansion in the eigenbasis of the Hamiltonian:

$$\Psi(\mathbf{R}, \tau) = \sum_{n=0}^{\infty} c_n \phi_n(\mathbf{R})\, e^{-E_n \tau}, \tag{B.3}$$

where E_n and ϕ_n are the eigenenergies and eigenfunctions, respectively. Using the imaginary-time formalism the solution becomes a decaying exponential. As τ increases, the excited-state contributions rapidly decay, and the only prevailing component is the ground-state. We are essentially filtering out all contributions, but the ground-state allows us to finally get the ground-state wavefunction:

$$\Psi(\mathbf{R}, \tau) \propto \phi_0(\mathbf{R})\, e^{-E_0 \tau}. \tag{B.4}$$

To solve this equation numerically, standard integration methods such as the Euler or Crank–Nicolson scheme can be used. However, for systems with more than a few particles, directly evolving the full wavefunction becomes computationally impractical due to the exponential growth of the Hilbert space. In such cases, stochastic approaches like Variational Monte Carlo (VMC) or Diffusion Monte Carlo (DMC) methods are typically used to prevent this limitation.

B.2 Variational Monte Carlo Method

The Variational Monte Carlo (VMC) method (Ref. [TAU16]) serves as a common first approach for many-body quantum mechanics calculations due to its flexibility and relatively low computational cost compared to exact diagonalization or other high-dimensional methods.
VMC is a stochastic technique that provides approximations—rather than exact calculations—of properties for stationary quantum states, provided we have a suitable trial wavefunction.
The method exploits the variational principle of quantum mechanics. This principle states that for any normalized trial wavefunction Ψ_T, the energy expectation value establishes an upper bound on the true ground-state energy:

$$\langle \Psi_T | H | \Psi_T \rangle \geq E_0, \tag{B.5}$$

where equality holds if Ψ_T is the true ground-state of the system.
This variational bound motivates one of the main applications of VMC method: the optimization of the parameters of a trial wavefunction that best approximates the true ground-state. We typically use a parametrized ansatz $\Psi_T(\mathbf{R}; \boldsymbol{\alpha})$, which depends on one or more variational parameters $\boldsymbol{\alpha}$. Through iterative VMC simulations, these parameters are systematically adjusted to minimize the estimated energy. The minimum obtained corresponds to the best approximation of the ground-state energy within the chosen ansatz. Moreover, the resulting

optimized wavefunction often serves as a starting point for more advanced Quantum Monte Carlo methods such as Diffusion Monte Carlo.
VMC transforms quantum mechanical expectation values into classical statistical sampling problems. For any observable O, we begin with the standard quantum mechanical expression:

$$\begin{aligned}\langle O\rangle &= \frac{\langle\Psi_T|O|\Psi_T\rangle}{\langle\Psi_T|\Psi_T\rangle} = \frac{\int \Psi_T^*(\mathbf{R})\, O\, \Psi_T(\mathbf{R})\, d\mathbf{R}}{\int |\Psi_T(\mathbf{R})|^2\, d\mathbf{R}} \\ &= \int \rho(\mathbf{R})\, O_{\text{local}}(\mathbf{R})\, d\mathbf{R} \approx \frac{1}{N_{\text{MC}}} \sum_{i=1}^{N_{\text{MC}}} O_{\text{local}}(\mathbf{R}_i),\end{aligned} \tag{B.6}$$

where we define the local observable $O_{\text{local}}(\mathbf{R}) = \frac{O\Psi_T(\mathbf{R})}{\Psi_T(\mathbf{R})}$ and sample configurations $\mathbf{R}_i$ from the probability distribution $\rho(\mathbf{R}) = |\Psi_T(\mathbf{R})|^2$ using Metropolis sampling.
This approach is fundamentally variational: we compute expectation values with respect to our chosen trial wavefunction, not the unknown true ground-state. The quality of our results depends entirely on how well Ψ_T approximates the actual ground-state. In the ideal case where our trial wavefunction exactly matches the true ground-state, the local energy (or other local observables) is constant throughout the simulation, and our estimate achieves exact accuracy with zero statistical variance.

B.3 Diffusion Monte Carlo Method

Even though the Variational Monte Carlo (VMC) method is a powerful tool that often provides an accurate approximation to the ground-state of a quantum system, it ultimately remains just that—an approximation. In practice, VMC frequently serves as the foundation for more advanced computational approaches. For instance, it provides a natural starting point for the Diffusion Monte Carlo (DMC) method, which, under suitable conditions, allows us to obtain the exact ground-state energy, Ref. [TAU16; Gui21; KFS96].
The DMC technique is built upon the same imaginary-time evolution framework introduced in Sec. B.1. However, instead of attempting to solve the high-dimensional partial differential equation directly, DMC method uses the Path Integral formulation of quantum mechanics, Ref. [FHS10]. This approach effectively projects out the ground-state from an initial wavefunction by stochastically evolving an ensemble of system configurations.
As a first step, we introduce a reference energy (E_R), which eventually will provide an alternative estimation for the ground-state energy, into the imaginary-time-dependent Schrödinger equation:

$$-\frac{\partial\Psi(\mathbf{R},\tau)}{\partial\tau} = -\frac{\hbar^2}{2m}\nabla^2_{\mathbf{R}}\Psi(\mathbf{R},\tau) + [V(\mathbf{R}) - E_R]\,\Psi(\mathbf{R},\tau). \tag{B.7}$$

The point of doing so is to stabilize the population size (wavefunction normalization) in the imaginary time propagation.
To further improve convergence and numerical stability, we introduce a trial wavefunction $\Psi_T(\mathbf{R})$ and consider the mixed distribution $f(\mathbf{R},\tau) = \Psi_T(\mathbf{R})\Psi(\mathbf{R},\tau)$. Multiplying Eq. (B.7) by $\Psi_T(\mathbf{R})$ leads to the importance-sampled evolution equation:

$$-\frac{\partial f(\mathbf{R},\tau)}{\partial\tau} = -D\nabla^2_{\mathbf{R}} f(\mathbf{R},\tau) + D\nabla_{\mathbf{R}}\cdot[F(\mathbf{R})f(\mathbf{R},\tau)] + [E_L(\mathbf{R}) - E_R]\, f(\mathbf{R},\tau), \tag{B.8}$$

where $D = \frac{\hbar^2}{2m}$ is the diffusion constant, $F(\mathbf{R})$ is the drift vector, and $E_L(\mathbf{R})$ is the local energy as previously defined in Eq. (B.6).
Our goal is to solve this equation in the long-time limit, $\tau \to \infty$, such that only the ground-state component of $\Psi(\mathbf{R},\tau)$ survives. In the context of importance sampling, this means

evolving $f(\mathbf{R}, \tau)$ until it is proportional to $\Psi_0(\mathbf{R})\Psi_T(\mathbf{R})$, where $\Psi_0(\mathbf{R})$ is the ground-state wavefunction.
To achieve this, we exploit the path integral formalism, in which the imaginary-time evolution of the wavefunction can be written as an average over all possible paths, weighted by the propagator:

$$\Psi(\mathbf{R}, \tau) = \int G(\mathbf{R}|\mathbf{R}'; \tau)\Psi(\mathbf{R}', 0)\, d\mathbf{R}', \tag{B.9}$$

where $G(\mathbf{R}|\mathbf{R}'; \tau) = \langle \mathbf{R}|U(\tau, 0)|\mathbf{R}'\rangle$ is the propagator.
Since the exact propagator is generally intractable for many-body systems, we employ the Suzuki-Trotter decomposition to approximate the short-time evolution operator. This decomposition allows us to treat the kinetic, drift, and potential/interaction terms of the Hamiltonian separately, even though they do not commute:

$$e^{-\Delta\tau\hat{H}} = e^{-\Delta\tau\hat{K}}e^{-\Delta\tau\hat{D}}e^{-\Delta\tau\hat{V}} + \mathcal{O}(\Delta\tau^2), \tag{B.10}$$

where $\hat{K} = -D\nabla^2_{\mathbf{R}}$, $\hat{D} = D\left[\nabla_{\mathbf{R}} \cdot F(\mathbf{R}) + F(\mathbf{R})\nabla_{\mathbf{R}}\right]$, and $\hat{V} = E_L(\mathbf{R}) - E_R$.
Due to the $\mathcal{O}(\Delta\tau^2)$ error in this approximation, it is necessary to use small time steps. To reach sufficiently large imaginary times, we discretize the evolution, applying the short-time propagator M times to reach a total time $\tau = M\Delta\tau$:

$$\Psi(\mathbf{R}_k, \tau) = \int ... \int \prod_{k=0}^{M-1} G_k(\mathbf{R}_{k+1}|\mathbf{R}_k; \Delta\tau)\Psi(\mathbf{R}_0, 0)\, d\mathbf{R}_1 \cdots d\mathbf{R}_{M-1}. \tag{B.11}$$

This discretized formulation gives way to a stochastic interpretation. We introduce an ensemble of configurations, or "walkers", each representing a possible realization of the system. At each time step, the propagator is applied to all walkers, and the collective evolution of the ensemble samples the desired distribution. In the long-time limit, the population of walkers converges to the mixed distribution proportional to the ground-state wavefunction.
To clarify the role of each operator in the evolution, we can decompose the application of the propagator into three consecutive steps:

- **Kinetic propagator:** Implements random Gaussian displacements, modeling diffusion in configuration space.
- **Drift propagator:** Introduces a deterministic drift, guiding walkers toward regions where the trial wavefunction is large, thus improving convergence if the trial wavefunction is close to the true ground-state.
- **Potential/Interaction (branching) propagator:** Acts as a weight, replicating walkers in low-energy regions and removing those in high-energy regions, relative to the reference energy E_R.

Repeated application of these three propagators to all walkers allows the ensemble to evolve according to the importance-sampled imaginary-time Schrödinger equation. Over many steps, the walker distribution converges to the mixed distribution proportional to the ground-state. However, the branching step can cause the walker population to diverge or vanish, making it crucial to dynamically adjust the reference energy to control the population size. Various population control schemes are available in the literature (see Ref. [TAU16; KFS96]), and this adjustment is particularly important before the system reaches equilibrium; after equilibration, the population remains mostly constant.

After ensuring population stability and convergence, we can estimate the ground-state energy by averaging the local energy over all walkers and over multiple time steps. This procedure provides an unbiased estimate of the true ground-state energy, exact within statistical uncertainty:

$$E_0 \simeq \frac{1}{M \cdot N} \sum_{i=1}^{M} \sum_{j=1}^{N} E_L(\mathbf{R}_{i,j}), \tag{B.12}$$

where M is the number of total steps performed after the system has reached equilibrium, and N is the number of walkers. This estimate has an associated statistical error, which is often computed using the blocking method defined in the next section.

Beyond the ground-state energy, DMC also allows the estimation of observables that do not commute with the Hamiltonian; in this case, DMC produces what are known as mixed estimators:

$$\frac{\langle \Psi_T | \hat{O} | \Psi_0 \rangle}{\langle \Psi_T | \Psi_0 \rangle}, \tag{B.13}$$

which do not, in general, correspond to the true ground-state expectation value. However, if the trial wavefunction is close to the true ground-state, improved estimates can be obtained by extrapolating between the DMC and VMC results. Two commonly used extrapolation formulas are:

$$\begin{aligned} \langle O \rangle_{\text{extr}}^{\text{linear}} &= 2 \langle O \rangle_{\text{DMC}} - \langle O \rangle_{\text{VMC}} \\ \langle O \rangle_{\text{extr}}^{\text{quadratic}} &= \frac{\langle O \rangle_{\text{DMC}}^2}{\langle O \rangle_{\text{VMC}}} \end{aligned} \tag{B.14}$$

The accuracy of these extrapolated estimators depends crucially on the quality of the trial wavefunction. For even greater accuracy, more sophisticated techniques can be employed, see Ref. [SBC02].

B.4 Statistical Error Analysis and Correlation Effects

Since Monte Carlo methods are inherently statistical, it is crucial to estimate the uncertainty when computing the mean of local observables. The naive estimate for the statistical error assumes that the sampled data is uncorrelated:

$$\epsilon_O^{\text{naive}} = \sqrt{\frac{\sigma_O^2}{N_{\text{MC}}}} = \sqrt{\frac{\langle O^2 \rangle - \langle O \rangle^2}{N_{\text{MC}}}}. \tag{B.15}$$

Nevertheless, both VMC and DMC are based on generating Markov chains, which are known to have correlations over consecutive steps. These correlations lead to an underestimation of the statistical error when Eq. (B.15) is used directly.

To account for these correlations, we use the *blocking method*, Ref. [FP89]. The sampled data is divided into N_{blocks} blocks of size M, and the observable is averaged within each block to generate a sequence of block averages $\bar{O}_k$. The variance of these block means then gives a more accurate estimation of the statistical error:

$$\epsilon_O^{\text{block}} = \sqrt{\frac{\text{Var}[\bar{O}_k]}{N_{\text{blocks}}}}. \tag{B.16}$$

Correlations within each block gradually decrease as the block size M increases until the estimated error $\epsilon_O^{\text{block}}$ finally saturates. The blocks are considered to be independent after this. To provide an accurate and unbiased error estimate without experiencing an excessive loss of sampling precision, we choose the ideal block size as the smallest M at which this saturation is obtained.

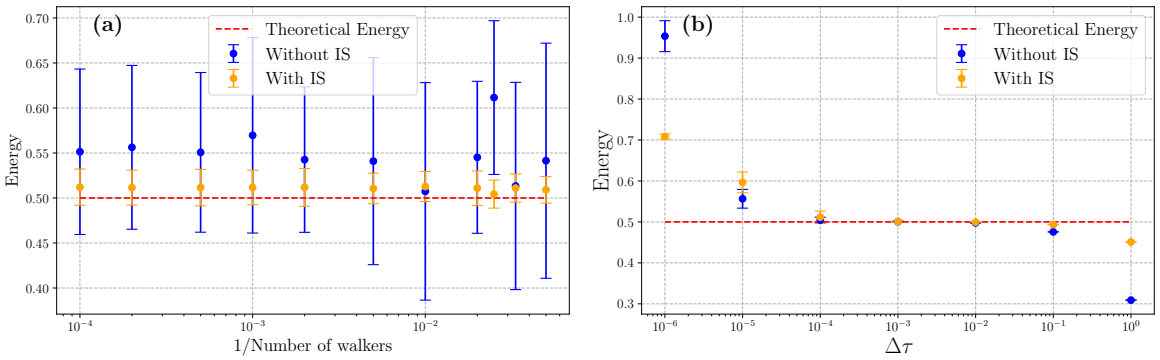

Figure 8: Diffusion Monte Carlo benchmark for the 1D harmonic oscillator.Panel (a): Mean energy E as a function of the inverse number of walkers N_{walkers}^{-1} at fixed time step $\Delta\tau = 10^{-4}$. We show results without importance sampling and with importance sampling using the guiding wavefunction $e^{-0.45x^2}$. Panel (b): Mean energy as a function of the time step $\Delta\tau$, again comparing the cases with and without importance sampling using the same trial wavefunction $e^{-0.45x^2}$. Statistical uncertainty is visualized by the error bars.

C Numerical Benchmarks

To ensure the reliability of our numerical methods, we carried out several numerical benchmarks throughout this master's thesis. The first benchmark involved simulating the Quantum Harmonic Oscillator, followed by the Ideal Fermi Gas and the Lieb-Liniger model. All of these models possess analytical solutions that serve as valuable references for validating our numerical results.

C.1 Harmonic Oscillator

To test and validate the Diffusion Monte Carlo (DMC) algorithm, we selected the quantum harmonic oscillator as a benchmark model due to its analytical tractability. The Hamiltonian for the one-dimensional harmonic oscillator, expressed in oscillator units, reads

$$H = \frac{1}{2}\left[-\frac{\partial^2}{\partial x^2} + x^2\right], \tag{C.1}$$

where x is measured in units of $x_0 = \sqrt{\hbar/(m\omega)}$ and energies are given in units of $\hbar\omega$. The exact ground-state energy for this system is $E_0 = 0.5$.

We first performed DMC simulations without importance sampling, which corresponds to using a constant trial wavefunction $\Psi_T(x) = 1$. To assess the benefits of importance sampling, we then compared these results to simulations using a Gaussian trial wavefunction $\Psi_T(x) = e^{-0.45x^2}$.

To characterize the performance and convergence of the DMC algorithm, we systematically varied both the number of walkers and the time step $\Delta\tau$. In the first study, we fixed $\Delta\tau = 10^{-4}$ and computed the energy as a function of the inverse number of walkers N_{walkers}^{-1}. In the second study, we fixed the number of walkers and examined the dependence of the energy estimate on $\Delta\tau$. These results are summarized in Figure 8, with the exact ground-state energy indicated by a red dashed line.

As shown in Fig. 8(a), increasing the number of walkers has little effect on the average value of the estimated energy, which remains close to the exact value even for relatively small populations. However, the statistical uncertainty is significantly reduced when importance sampling is introduced. This approach systematically suppresses fluctuations and yields

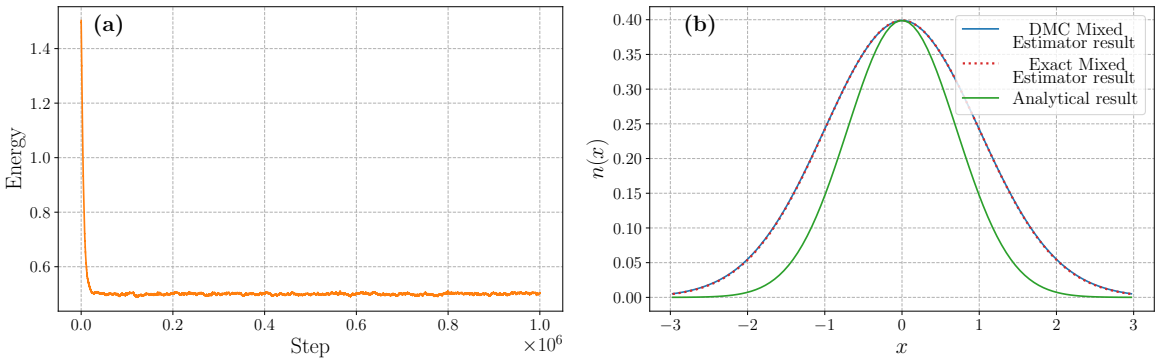

Figure 9: Convergence of the ground-state energy and density profile for the harmonic oscillator using DMC. Panel (a): Evolution of the estimated ground-state energy during the DMC simulation with 50,000 walkers and time step $\Delta\tau = 10^{-4}$. Panel (b): Density profile obtained from DMC compared to the theoretical ground-state density $|\psi_0(x)|^2 = \frac{1}{\sqrt{2\pi}} e^{-x^2}$.

tighter error bars, particularly when the chosen trial wavefunction closely resembles the true ground-state.

Panel (b) of Fig. 8 shows the dependence of the estimated energy on the time step $\Delta\tau$. For large time steps ($\Delta\tau \gtrsim 10^{-2}$), discretization errors become significant, causing a systematic overestimation of the ground-state energy. As $\Delta\tau$ is decreased, the estimated energies converge towards the exact value, with optimal performance typically observed in the range $\Delta\tau \sim 10^{-4}$ to 10^{-3}. For very small time steps ($\Delta\tau \lesssim 10^{-5}$), convergence can become limited by the total simulation time, as equilibration takes longer and the system may not fully project onto the ground-state. This is not a finite-size effect, but rather a consequence of insufficient imaginary-time propagation. Again, the use of importance sampling improves the rate of convergence and enables accurate results even for moderately large time steps.

The evolution of the estimated ground-state energy throughout the simulation is shown in Fig. 9(a). As expected, the system rapidly relaxes toward the ground-state energy, exhibiting small statistical fluctuations due to the stochastic nature of the DMC algorithm.

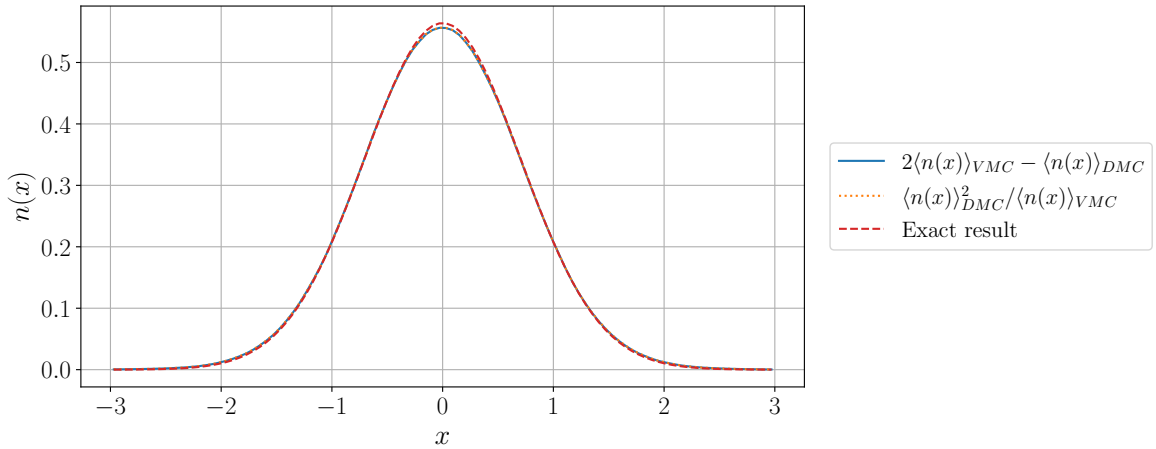

Figure 10: Extrapolation is performed using both forms of Eq. (B.14), which in this case yield identical results. The blue solid line corresponds to the first extrapolation method, the orange dotted line to the second, and the green dashed line represents the exact analytical density for the harmonic oscillator.

Figure 9(b) shows the density profile obtained from the DMC simulation. This is compared

to two theoretical results: the exact ground-state density,

$$\frac{1}{\sqrt{2\pi}} e^{-x^2},$$

and the expected mixed estimator,

$$\frac{1}{\sqrt{2\pi}} e^{-x^2/2},$$

which arises from the product of the trial wavefunction Ψ_T and the exact ground-state wavefunction. As we can see, the DMC result agrees well with the mixed estimator curve, confirming the correctness and consistency of the simulation. The observed deviation from the exact ground-state density is expected due to the use of mixed estimators, which are biased toward the chosen trial wavefunction Ψ_T.
In Fig. 10, we show the implementation of the extrapolation of mixed estimators in DMC as defined in Eq. (B.14). Both extrapolation methods show results that are very close to the exact density profile, which is expected, given that the trial wavefunction used in the simulation closely resembles the true ground-state wavefunction.

C.2 Lieb-Liniger Model

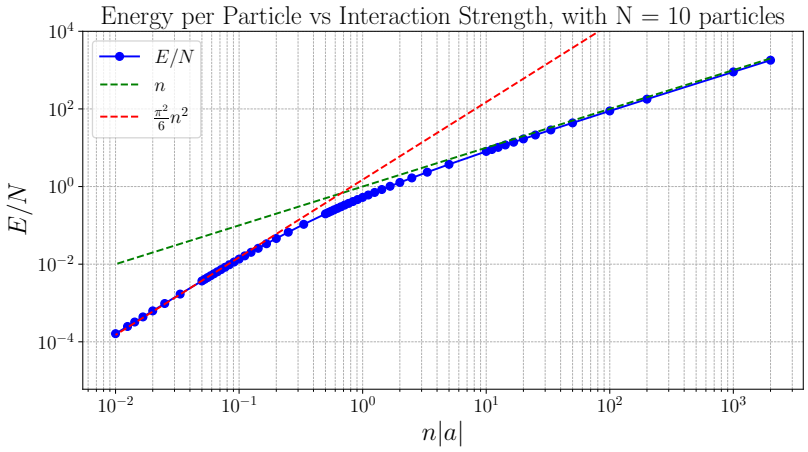

Figure 11: Results obtained for $N = 10$ particles using only the contact-interaction component of the trial wavefunction. For weak repulsive interactions, the energy per particle follows the expected scaling from the mean-field Gross–Pitaevskii approximation. In the strongly interacting regime, the system approaches the Tonks–Girardeau limit and the energy per particle recovers the corresponding theoretical dependence.

Number of particles	$E/N_{\text{Bethe ansatz}}$	E/N_{VMC}	Relative error (%)	E/N_{DMC}	Relative error (%)
2	0.3700869709968962	0.37008694 ± 10^{-17}	3×10^{-6} %	0.37008694 ± 10^{-17}	3×10^{-6} %
4	0.4848539578705682	$0.48645 \pm (3 \times 10^{-5})$	0.3 %	0.4850 ± 0.0002	0.03 %
8	0.5149998755337507	$0.52088 \pm (5 \times 10^{-5})$	1.1 %	0.5145 ± 0.0008	0.1 %
12	0.5206380308995034	$0.52848 \pm (6 \times 10^{-5})$	1.5 %	0.519 ± 0.002	0.3 %

Table 2: Comparison of the energy per particle in the Lieb–Liniger model computed using Diffusion Monte Carlo (DMC) and Variational Monte Carlo (VMC) with the trial wavefunction $\prod_{i<j} \cos\left[k_c\left(|x_i - x_j| - \frac{L}{2}\right)\right]$, against the exact Bethe ansatz result. The DMC results closely match the exact values, with deviations within the accepted error range. As expected, the VMC method slightly overestimates the energy.

To validate our numerical implementation in the presence of short-range interactions, we benchmark the Quantum Monte Carlo methods against the exactly solvable Lieb–Liniger

model [LL63], which describes a one-dimensional gas of bosons with contact interactions. The ground-state energy in this model depends solely on the dimensionless interaction parameter $\gamma = 2/\rho_0|a_{1D}|$, where $\rho_0 = N/L$ is the density and a_{1D} is the 1D scattering length.
Figure 11 shows the energy per particle for a system of $N = 10$ bosons interacting only through the contact component of the trial wavefunction. In the weakly interacting regime, our results reproduce the mean-field Gross–Pitaevskii limit, while in the strongly interacting regime ($\gamma \gg 1$), the system approaches the Tonks–Girardeau limit, where bosons mimic the behavior of non-interacting fermions due to the impenetrability induced by strong repulsion. To quantitatively assess the accuracy of our methods, Table 2 compares the energy per particle obtained from Variational and Diffusion Monte Carlo with the exact Bethe ansatz solution for various system sizes. The DMC method yields excellent agreement with the exact results, with relative errors typically below 0.3% across the board. As expected, the VMC method systematically overestimates the ground-state energy, but remains within a few percent of the exact value, validating the quality of the chosen trial wavefunction. These results confirm the reliability of our numerical implementation for simulating contact-interacting bosons and provide a robust benchmark for interpreting the more complex scenarios involving cavity-mediated long-range interactions.

D Contact Interaction via Bethe–Peierls Boundary Condition (1D)

In one dimension, a zero-range contact interaction between two particles is modeled as

$$U(x) = \frac{2\hbar^2}{a_{1D}}\delta(x), \tag{D.1}$$

where $x = x_1 - x_2$ is the relative coordinate, m is the mass, and a_{1D} is the 1D scattering length. In this case, we have assumed that the two particles interacting have the same mass m.
To avoid dealing with the singularity of the delta function directly in numerical simulations, we instead impose a boundary condition on the wavefunction, known as the *Bethe–Peierls boundary condition*. This condition can be derived by integrating the relative-coordinate Schrödinger equation:

$$\left[-\frac{\hbar^2}{2\mu}\frac{d^2}{dx^2} - \frac{\hbar^2}{\mu a}\delta(x)\right]\Psi(x) = E\Psi(x) \tag{D.2}$$

across a small symmetric interval $x \in [-\epsilon, \epsilon]$. Performing the integration:

$$-\frac{\hbar^2}{2\mu}\int_{-\epsilon}^{\epsilon}\Psi''(x)\,dx - \frac{\hbar^2}{\mu a}\int_{-\epsilon}^{\epsilon}\delta(x)\,\Psi(x)\,dx = E\int_{-\epsilon}^{\epsilon}\Psi(x)\,dx. \tag{D.3}$$

In the limit $\epsilon \to 0$, the right-hand side vanishes. The left-hand side yields:

$$-\frac{\hbar^2}{2\mu}\left[\Psi'(0^+) - \Psi'(0^-)\right] - \frac{\hbar^2}{\mu a}\Psi(0) = 0. \tag{D.4}$$

Assuming a symmetric bosonic wavefunction ($\Psi'(0^+) = -\Psi'(0^-)$), we obtain:

$$\frac{\Psi'(0^+)}{\Psi(0)} = -\frac{1}{a}, \tag{D.5}$$

which defines the Bethe–Peierls boundary condition in 1D. It captures the correct short-range behavior of the wavefunction in the presence of a delta potential.

A simple symmetric wavefunction satisfying this condition is

$$f_{2B}(x) = \cos\left[k_c\left(|x| - \frac{L}{2}\right)\right], \tag{D.6}$$

with the derivative

$$f'_{2B}(x) = -k_c \sin\left[k_c\left(|x| - \frac{L}{2}\right)\right]. \tag{D.7}$$

Evaluating at $x = 0$, we find

$$\frac{f'_{2B}(0^+)}{f_{2B}(0)} = -k_c \tan\left(\frac{k_c L}{2}\right), \tag{D.8}$$

which, matched to the boundary condition, gives the relation:

$$k \tan\left(\frac{kL}{2}\right) = -\frac{1}{a}. \tag{D.9}$$

This leads to the following contact-interaction contribution to the trial wavefunction:

$$\Psi^{(\mathrm{B})}_{\mathrm{SR}}(x_1, \ldots, x_N) = \prod_{i<j} \cos\left[k_c\left(|x_i - x_j| - \frac{L}{2}\right)\right]. \tag{D.10}$$

E Logarithmic derivatives for local energy and drift force calculations

In variational or diffusion Monte Carlo methods, evaluating the local energy efficiently and accurately is essential. When the trial wavefunction is constructed as a product over pairwise terms, it is particularly advantageous to work with its logarithmic derivatives. This reformulation simplifies the computation of both the gradient and Laplacian of the wavefunction, which are needed for the kinetic energy and the drift force:

$$\begin{aligned} \frac{\nabla_k^2 \Psi}{\Psi} &= \nabla_k^2 \log \Psi + (\nabla_k \log \Psi)^2, \\ \mathbf{F}_k &= 2\nabla_k \log \Psi. \end{aligned}$$

The trial wavefunction used in this Thesis has three different contributions:

$$\Psi^{(\mathrm{B})}_{\mathrm{LR}}(x_1, ..., x_N) = \prod_{i<j} \psi_2(x_i, x_j), \tag{E.1}$$

$$\Psi^{(\mathrm{B})}_{\mathrm{SR}}(x_1, ..., x_N) = \prod_{i<j} \sin\left(\frac{\pi}{L}(x_i - x_j)\right), \tag{E.2}$$

$$\Psi^{(\mathrm{F})}(x_1, ..., x_N) = \prod_{i<j} \cos\left[k_{\mathrm{c}}\left(|x_i - x_j| - \frac{L}{2}\right)\right], \tag{E.3}$$

where (LR) denotes the cavity-induced long-range contribution, (SR) refers to the short-range interaction. The superscripts (B) and (F) indicate whether the corresponding term is symmetric (bosonic) or antisymmetric (fermionic) under particle exchange.
Below we provide the explicit expressions for the gradient and Laplacian of the logarithm of Ψ, split by each contribution:

1. **Interpolated long-range term**:

$$\log \Psi_{\mathrm{LR}}^{(\mathrm{B})} = \sum_{i<j} \log \psi_2(x_i, x_j), \tag{E.4}$$

$$\nabla_k \log \Psi_{\mathrm{LR}}^{(\mathrm{B})} = \sum_{j\neq k} \frac{\nabla_k \psi_2(x_k, x_j)}{\psi_2(x_k, x_j)}, \tag{E.5}$$

$$\nabla_k^2 \log \Psi_{\mathrm{LR}}^{(\mathrm{B})} = \sum_{j\neq k} \left[\frac{\psi_2(x_k, x_j)\nabla_k^2 \psi_2(x_k, x_j) - (\nabla_k \psi_2(x_k, x_j))^2}{\psi_2(x_k, x_j)^2} \right], \tag{E.6}$$

where $\psi(x_k, x_j)$ denotes the pairwise wavefunction component evaluated using spline interpolation. Although the spline is constructed numerically, its derivatives can be computed analytically from the interpolation basis, providing accurate and efficient expressions for the drift and local energy in the simulation.

2. **Fermi-statistics term**:

$$\nabla_k \log \Psi^{(\mathrm{F})} = \sum_{j\neq k} \frac{\pi}{L} \cot\left(\frac{\pi}{L}(x_k - x_j)\right), \tag{E.7}$$

$$\nabla_k^2 \log \Psi^{(\mathrm{F})} = -\sum_{j\neq k} \left(\frac{\pi}{L}\right)^2 \csc^2\left(\frac{\pi}{L}(x_k - x_j)\right). \tag{E.8}$$

3. **Contact-interaction term**:

$$\nabla_k \log \Psi_{\mathrm{SR}}^{(\mathrm{B})} = -k_{\mathrm{cont}} \sum_{j\neq k} \tan\left(k_{\mathrm{cont}}\left(|x_k - x_j| - \frac{L}{2}\right)\right) \cdot \mathrm{sgn}(x_k - x_j), \tag{E.9}$$

$$\nabla_k^2 \log \Psi_{\mathrm{SR}}^{(\mathrm{B})} = -k_{\mathrm{cont}}^2 \sum_{j\neq k} \sec^2\left(k_{\mathrm{cont}}\left(|x_k - x_j| - \frac{L}{2}\right)\right). \tag{E.10}$$

F Comparing energy results using VMC and DMC methods

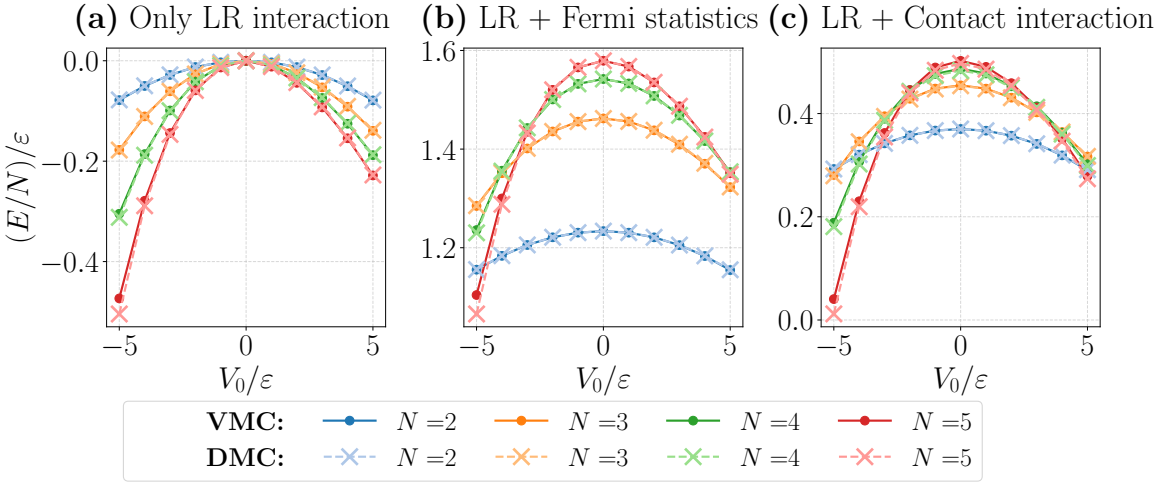

Figure 12: Comparison of the energy obtained using Variational Monte Carlo (VMC) with the trial wavefunction specified in Table 1, and the energy obtained using Diffusion Monte Carlo (DMC) using the same wavefunction as the guiding function. Panel (a): Long-range interaction only. Panel (b): Combined contact and long-range interactions. Panel (c): Long-range interaction with fermionic statistics.

Figure 12 compares the ground-state energies obtained using Variational Monte Carlo (VMC) and Diffusion Monte Carlo (DMC) for different interaction regimes. In all panels, the same trial wavefunction (summarized in Table 1) is used for both methods, serving as the variational ansatz in VMC and as the guiding function in DMC. As expected, the DMC energies are systematically lower than the VMC ones, in agreement with the variational principle. The energy difference provides an estimate of the quality of the trial wavefunction.

In the purely long-range case Fig. 12 (a), the two methods yield very similar results, indicating that the trial wavefunction accurately captures the dominant correlations. The discrepancy becomes more pronounced in the presence of contact interactions Fig. 12 (b), suggesting that short-range correlations are not fully described by the variational ansatz. In the fermionic case Fig. 12 (c), the fixed-node constraint is imposed by the nodal structure of the guiding wavefunction, and the observed energy difference reflects both the quality of this constraint and the accuracy of the trial state.

In general, as the number of particles increases, the VMC energy deviates more from the DMC result. This deviation also grows with increasing interaction strength V_0, particularly in the attractive regime, where the many-body behavior becomes more complex and the trial wavefunction fails to fully capture the underlying physics.

G Structure Factor Comparison: Contact Interaction vs. Contact and Long-Range Interaction

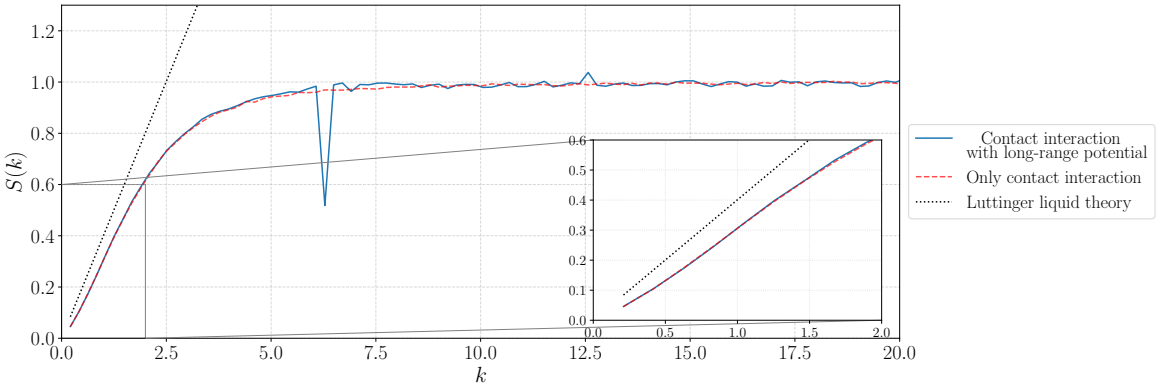

Figure 13: Static structure factor comparison between three cases: contact interaction only (dashed red line), contact plus cavity-mediated long-range interaction (solid blue line), and the theoretical prediction from Luttinger liquid theory (black dotted line).

Figure 13 shows that the cases with only contact interaction and with additional cavity-mediated long-range interaction closely coincide at low momentum. When compared to the theoretical prediction from Luttinger liquid theory, both curves deviate, indicating that the discrepancy arises from the use of an approximate variational wavefunction rather than from the presence of the cavity-mediated interaction.